Polymer-extracted structure of the mechanosensitive channel MscS reveals the role of protein-lipid interactions in the gating cycle

Elissa Moller [1,2,3], Madolyn Britt [2,3], Fei Zhou [1], Hyojik Yang [4], Andriy Anshkin[3], Robert Ernst [4], Sergei Sukharev [2,3,5,#], Doreen Matthies [1,#]

[1] Unit on Structural Biology, Division of Basic and Translational Biophysics, *Eunice Kennedy Shriver* National Institute of Child Health and Human Development, National Institutes of Health, Bethesda, MD, USA.

[2] Biophysics Graduate Program, University of Maryland, College Park, MD, USA.

[3] Department of Biology, University of Maryland, College Park, MD, USA.

[4] Department of Microbial Pathogenesis, University of Maryland, Baltimore, MD, USA.

[5] Institute for Physical Science and Technology, University of Maryland, College Park, MD, USA.

Correspondence to Sergei Sukharev (sukharev@umd.edu) and Doreen Matthies (Doreen.Matthies@nih.gov)

Running title: Mechanosensitive channel MscS in Glyco-DIBMA

Keywords: native nanodiscs, cryo-EM, mechanosensation, polymer, membrane protein structure, protein-lipid interaction

Abbreviations: mechanosensitive channel (MSC), mechanosensitive channel of small conductance (MscS), transmembrane (TM), electron microscopy (EM), Blue Native (BN)

Abstract

Membrane protein structure determination is not only technically challenging but is further complicated by the removal or displacement of lipids, which can result in non-native conformations or a strong preference for certain states at the exclusion of others. This is especially applicable to mechanosensitive channels (MSC's) that evolved to gate in response to subtle changes in membrane tension transmitted through the lipid bilayer. *E. coli* MscS, a model bacterial system, is an ancestral member of the large family of MSCs found across all phyla of walled organisms. As a tension sensor, MscS is very sensitive and highly adaptive; it readily opens under super-threshold tension and closes under no tension, but under lower tensions, it slowly inactivates and can only recover when tension is released. However, existing cryo-EM structures do not explain the entire functional gating cycle of open, closed, and inactivated states. A central question in the field has been the assignment of the frequently observed non-conductive conformation to either a closed or inactivated state. Here, we present a 3 Å MscS structure in native nanodiscs obtained with Glyco-DIBMA polymer extraction, eliminating the lipid removal step that is common to all previous structures. Besides the protein in the non-conductive conformation, we observe well-resolved densities of four endogenous phospholipid molecules intercalating between the lipid-facing and pore-lining helices in preferred orientations. Mutations of positively charged residues coordinating these lipids inhibit MscS inactivation, whereas removal of a negative charge near the lipid-filled crevice increases inactivation. The functional data allows us to assign this class of structures to the inactivated state. This structure reveals preserved lipids in their native locations, and the functional effects of their destabilization illustrate a novel inactivation mechanism based on an uncoupling of the peripheral tension-sensing helices from the gate.

Introduction

MscS is an essential low threshold osmolyte release valve that was first identified in bacteria (Levina et al., 1999) but its multiple homologs are now found in all clades of walled organisms (Hamilton et al., 2015b; Haswell et al., 2011; Pivetti et al., 2003). In prokaryotes, MscS assists in regulating turgor pressure, thereby enabling osmotic shock survival and providing environmental stability. In eukaryotes, MscS homologs fulfill multiple sensory functions (Hamilton et al., 2015a; Jojoa-Cruz et al., 2022) and impart osmotic stability to internal organelles (Veley et al., 2012; Wilson et al., 2011). The 'successful' structural design of MscS and its adaptive behavior deserve detailed analysis, as it represents much more than a prokaryotic system.

Escherichia coli MscS, residing in the cytoplasmic membrane, is a 217 kDa homo-heptamer with each 287 residue (31 kDa) subunit comprising three transmembrane helices and a large hollow cytoplasmic domain. It gates directly by tension transmitted through the surrounding lipid bilayer (Sukharev, 2002). MscS's behavior in the mechanically stressed membrane is highly adaptive: it robustly opens in response to abruptly applied super-threshold tension but gradually inactivates under prolonged action of near-threshold tension. Its functional cycle comprises the closed, open, and inactivated states, the latter being non-conductive and tension insensitive (Akitake et al., 2007; Akitake et al., 2005). There are two separate opening and inactivation pathways, both originating from the closed state. Each pathway is characterized by its own tension sensitivity, in-plane protein area expansion, and kinetics (Çetiner et al., 2018; Kamaraju et al., 2011). The opening-closing transitions are sharply tension-dependent and can be very fast (Boer et al., 2011). In contrast, the inactivation and recovery transitions are slow and sensitive to the lipid environment and the nature of lipid-anchoring sidechains (Britt et al., 2024).

While there are many *E. coli* MscS structures (Angiulli et al., 2020; Bass et al., 2002; Flegler et al., 2021; Park et al., 2023; Rasmussen et al., 2019; Reddy et al., 2019; Wang et al., 2008; Zhang et al., 2021), they do not fully explain the entire three-state functional cycle, and all of them were initially subjected to de-lipidation by detergent solubilization. There are two overarching classes of structures: (1) a non-conductive state with the transmembrane (TM) helices tilted inward at the top and splayed away from the pore lining helix at the cytoplasmic side and (2) an expanded semi-conductive state. These protein conformations are highly dependent on the surrounding lipid environment, with the presence of regular lipids resulting in the non-conductive state and high detergent concentrations yielding the expanded semi-conductive state. The lipidation of the channel causes a large rearrangement of the TM helices and can be induced simply by adding lipids to form a mixed micelle rather than retaining the pure detergent micelle (Flegler et al., 2021). This splayed structure overlays quite well with the nanodisc structures using full-

length lipids (Rasmussen et al., 2019; Reddy et al., 2019). Using artificially short acyl chains can result in a structure more similar to the semi-conductive state (Park et al., 2023; Zhang et al., 2021).

Lipids have been found in several MscS structures (Flegler et al., 2021; Rasmussen et al., 2019; Reddy et al., 2019; Zhang et al., 2021), which triggered many speculations on their role in the MscS gating mechanism (Park et al., 2023; Pliotas et al., 2015; Reddy et al., 2019). MscS opens with slightly different tension sensitivities in reconstituted soybean lipids when compared to the more native spheroplast lipid environment (Belyy et al., 2010b; Sukharev, 2002). While MscS opens robustly in most tested environments (Nomura et al., 2012; Ridone et al., 2015; Sukharev et al., 1993), the slow inactivation process and its dependence on the lipid anchoring residues suggests that lipids may be inseparable players in the mechanism of MscS inactivation or maintenance of the active state. Both structural and functional data are needed to explain their role.

During a standard membrane protein purification, lipids are typically removed from membrane proteins prior to structural studies (Supplemental Figure 1). Detergents are the most commonly used (Supplemental Figure 1B), but they are a poor mimic for the lipid bilayer environment and can cause structural changes or even denaturation of membrane proteins (Johansen et al., 2023). Lipids can be reintroduced in the form of mixed micelles, liposomes, or synthetic nanodiscs (Supplemental Figure 1C-E), but extraction from the native membrane with detergent is still a prerequisite step (Johansen et al., 2023). A more recent approach is to use polymers to extract membrane proteins out of a lipid bilayer (Ratkeviciute et al., 2021). The main advantage of using polymers rather than detergents for extraction is the absence of the detergent solubilization and de-lipidation step (Supplemental Figure 1F). Direct membrane disruption via polymer solubilization to form native nanodiscs was first shown for styrene maleic acid (SMA) (Knowles et al., 2009) and widely used for functional studies prior to its use for high-resolution cryo-EM reconstruction of Alternative complex III (Sun et al., 2018) and AcrB (Qiu et al., 2018). Many different polymers are now commercially available; the polymers used in this study are Glyco-DIBMA (Danielczak et al., 2022), SMALP 200 (Knowles et al., 2009), and CyclAPol C_8-C_0-50 (Higgins et al., 2021). Glyco-DIBMA is a diisobutylene-maleic acid polymer with an additional glycosylation. SMALP 200 is a poly-styrene-maleic anhydride polymer with hydrophobic styrene groups and reactive, functionalizable anhydrides. CyclAPol C_8-C_0-50 is a cycloalkane-modified amphiphilic polymer. Structural studies require careful consideration of the lipid environment in terms of what co-purifies with the protein and in what stable positions the associated lipids are found. Different solubilization approaches may yield different outcomes, especially when amphipathic polymers completely replace detergents.

In the present work we have attempted to use three polymers to solve the structure of MscS using single-particle cryo-EM. Attempts to use SMALP 200 or CyclAPol C8-C0-50 resulted in only the cytoplasmic domain of MscS resolved but not the TM region. However, we were able to solve the structure of MscS in Glyco-DIBMA to 3 Å. From this structure we were able to identify the specific positions and conformations of four lipids intercalating between the lipid-facing TM1-TM2 helical pairs and the gate-forming TM3s. The importance of TM2-TM3 interactions for proper MscS gating has been suggested previously (Belyy et al., 2010a). The resolution was sufficient to determine the lipid-coordinating residues. Mutations of these residues were functionally tested by patch-clamp and showed clear inactivation phenotypes. The data strongly suggest that the splayed non-conductive conformation represents the inactivated state. We discuss the mechanistic role of the intercalated lipids in relation to the spatial characteristics of the system as well as the physical forces that may drive the inactivation and recovery transitions in MscS.

Methods

MscS Expression and Inner Membrane Isolation

E. coli MscS wild-type (WT) was expressed in MJF465 cells (Frag1 ΔmscL::Cm, ΔyggB, ΔmscK::kan) (Levina et al., 1999) from the pB10d vector, a modified pB10b plasmid (Iscla et al., 2008). The plasmid is IPTG inducible with the lac UV5 and lacIq promoters, confers ampicillin resistance, and includes a C-terminal 6-His tag on the MscS gene. It uses the high-copy-number ColE1/pMB1/pBR322/pUC origin of replication and the T7 bacteriophage ribosome binding site. The MJF465 strain originated from the I. Booth laboratory (University of Aberdeen, Aberdeen, UK) and was provided by Dr. Samantha Miller (University of Aberdeen). A single colony of the plasmid containing strain was inoculated into 35 mL Luria Bertani (LB) media supplemented with Ampicillin (Amp) and grown overnight. 5 mL of the overnight culture was sub-cultured into six 2-L flasks containing 1 L LB supplemented with 100 µg/mL Amp and grown for 2 hours shaking at 225 rpm at 30ºC to an OD600 of approximately 0.3 before induction with 1 mM IPTG for an additional 3 hours to a final OD600 of 2.0. When the target OD was achieved cells were placed on ice to prevent further growth, pelleted at 7,000 rpm using Sorvall GSA rotor for 15 min at 4ºC, and resuspended in French Press Buffer (20 mM Tris/HCl pH 7.6, 150 mM NaCl) supplemented with 10 mg lysozyme and 200 µL saturated PMSF in EtOH to 30 mL total volume before rupturing with a French press. Unbroken cells were pelleted by centrifugation at 10,000 rpm using Eppendorf F-34-6-38 rotor for 15 min at 4ºC, supernatant was then ultracentrifuged at 25,000 rpm using Beckman SW28 rotor (112,398.1 x g) for 1 hr at 4ºC to pellet membranes. Supernatant was discarded and membranes were resuspended in 20% [w:v] sucrose and 5 mM EDTA and homogenized before being placed on top of a 3-step sucrose gradient of 0.77 M, 1.44 M, and 2.02 M prepared in Gradient Buffer (20

mM HEPES pH 7.2, 5 mM EDTA) and ultracentrifuged at 25,000 rpm using Beckman SW28 rotor (112,398.1 x g) for 16 hrs at 8ºC. The inner membranes were harvested from the upper band of the gradient by puncturing the tube wall with a syringe needle, diluted in Gradient Buffer with no sucrose to 70 mL total volume, and ultracentrifuged at 25,000 rpm using Beckman SW28 rotor (112,398.1 x g) for 1 hr at 4ºC to re-pellet membranes. The membrane pellets were flash frozen in liquid nitrogen and stored at -80ºC until use.

Glyco-DIBMA Extraction and Affinity Purification

E. coli inner membranes were resuspended to 10 mg/ml in Membrane Buffer 1 (20 mM HEPES pH 7.4; 100 mM NaCl) and homogenized before the addition of 0.5% [w:v] of solid Glyco-DIBMA (Cube Biotech). The first condition (Glyco-DIBMA #1) was allowed to solubilize overnight at 4ºC on the tube revolver while the second condition (Glyco-DIBMA #2) was allowed to solubilize for 2 hrs at room temperature on the rotisserie. The insoluble fraction was then pelleted by ultracentrifugation at 25,000 rpm using Beckman SW28 rotor (112,400 x g) for 35 min at 4ºC. The supernatant was then diluted 1:5 to improve binding efficiency and incubated overnight on the rotisserie at 4ºC with TALON Cobalt Resin (Takara Bio). The next day the resin was washed with 10 column volumes of Membrane Buffer 1, 10 column volumes of Wash Buffer (20 mM HEPES pH 7.4, 100 mM NaCl, 10% glycerol [v:v]) with 10 mM imidazole, 5 column volumes Wash Buffer with 20 mM imidazole, and 5 column volumes of Wash Buffer with 40 mM imidazole before elution with Elution Buffer (20 mM HEPES pH 7.4, 100 mM NaCl, 10% glycerol [v:v], 350 mM imidazole). Elution fractions were then dialyzed with Membrane Buffer 1 overnight to remove imidazole and glycerol and concentrated the following day using a 100 kDa ultrafiltration membrane (Amicon) to desired concentration for cryo-EM grid preparation.

SMALP 200 Extraction and Affinity Purification

E. coli inner membranes were resuspended to 20 mg/mL in Membrane Buffer 2 (50 mM Tris/HCl pH 8.0, 500 mM NaCl, 10% glycerol [v:v]) and homogenized before the addition of 1% [w:v] of SMALP 200 (Orbiscope) and allowed to solubilize for 2 hrs at room temperature on the rotisserie. SMALP 300 was also attempted but did not successfully solubilize. The insoluble fraction was then pelleted by ultracentrifugation at 25,000 rpm using Beckman SW28 rotor (112,400 x g) for 35 min at 4ºC. The supernatant was then diluted 1:4 to improve binding efficiency and incubated overnight on the rotisserie at 4ºC with TALON Cobalt Resin (Takara Bio). The next day the resin was washed with 10 column volumes of Membrane Buffer 2 and 10 column volumes of Membrane Buffer 2 with 20 mM imidazole before elution with Membrane Buffer 2 with 300 mM imidazole. Elution fractions were then dialyzed with Purification Buffer (20 mM Tris/HCl pH 8.0, 250 mM NaCl, 5% glycerol [v:v]) overnight to remove

imidazole and concentrated the following day using a 100 kDa ultrafiltration membrane (Amicon) to desired concentration for cryo-EM grid preparation.

CyclAPol C_8-C_0-50 Extraction and Affinity Purification

E. coli inner membranes were resuspended to 10 mg/mL in Purification Buffer and homogenized before the addition of 0.1% [w:v] of CyclAPol C_8-C_0-50 and allowed to solubilize for 2 hrs at room temperature on the rotisserie. CyclAPol C_8-C_0-50 (Higgins et al., 2021) was provided by Manuela Zoonens (Université de Paris and Institut de Biologie Physico-Chimique, Paris, France) and is now commercially available as Ultrasolute Amphipol 18 (Cube Biotech). The insoluble fraction was then pelleted by ultracentrifugation at 25,000 rpm using Beckman SW28 rotor (112,398.1 x g) for 35 min at 4ºC and the supernatant was incubated overnight on the rotisserie at 4ºC with TALON Cobalt Resin (Takara Bio). The next day the resin was washed with 10 column volumes of Purification Buffer and 10 column volumes of Purification Buffer with 10 mM imidazole before elution using Purification Buffer with 300 mM imidazole. Elution fractions were then dialyzed with Purification Buffer overnight to remove imidazole and concentrated the following day using a 100 kDa ultrafiltration membrane (Amicon) to desired concentration for cryo-EM grid preparation.

Protein Validation using SDS-PAGE, Western Blot, and Blue Native-PAGE

Protein fractions were resolved and analyzed using SDS-PAGE, Western Blot, and BN-PAGE. For SDS-PAGE samples were prepared with 4X Bolt LDS Sample Buffer (Invitrogen) and incubated at 80°C for 10 minutes before loading into 4-12% Bis-Tris gel (Invitrogen) with NuPAGE MOPS SDS Buffer (Invitrogen) and running at 80 V for 15 minutes followed by 200 V for 45 minutes on ice. SDS-gel was fixed and then stained with Colloidal Blue Stain (Invitrogen) overnight and de-stained in water and scanned the following day using Espson Perfection V850 Pro. For Western Blot, SDS-PAGE gel was transferred to PVDF membrane at 30 V for 45 min in NuPAGE Transfer Buffer (Invitrogen) and blocked with 4% BSA in TTBS [100 mM Tris/HCl pH 7.5, 150 mM NaCl, 0.1% Tween 20] for 1 hour, incubated with 0.1 µg/mL Anti-6X His tag antibody (abcam) in 2% BSA in TTBS for 1 hour, washed with TTBS and imaged with ChemiDoc (BioRad) using WesternBright (advansta). Note that the MscS monomer is 31 kDa but migrates faster than expected for its size. This is not unusual, as membrane proteins have been previously shown to have anomalous gel mobility (Rath et al., 2009). For BN-PAGE samples were prepared with NativePAGE Sample Buffer and 0.125% NativePAGE G-250 Sample Additive (Invitrogen) and loaded into a 4-16% Bis-Tris gel (Invitrogen) with NativePAGE Running Buffer and NativePAGE Cathode Buffer in the inner chamber (Invitrogen) before running at 150 V for 1 hour followed by 250 V for 1 hour on ice. Gel was fixed in 40% ethanol, 10% acetic acid microwaved for 1 minute and then

stained with Colloidal Blue Stain (Invitrogen) overnight and de-stained in water and scanned the following day. Gel images and Western Blots for each purification can be found in Supplemental Figures 2-4.

Negative Staining Electron Microscopy

3 µL of MscS sample at 0.3 mg/ml (30 times higher than MscS in detergents or mixed micelles of typically ~ 0.01 mg/mL) or polymer sample of 0.5%, 1%, and 0.1% for Glyco-DIBMA, SMALP 200, and CyclAPol C_8-C_0-50, respectively was applied to a glow discharged carbon coated 400 square mesh copper grid (CF400-CU, EMS) and incubated for 1 min at room temperature. The grid was then blotted by filter paper (Whatman Grade 2) and washed once with 3 µL of Nano-W negative staining solution (Nanoprobes) followed by incubation with 3 µL of Nano-W for 1 min. The grid was blotted to remove excess staining solution and air-dried by waving for an additional minute. Images were recorded using an FEI Tecnai T20 TEM operated at 200 kV with a direct electron detector K2 Summit (Gatan Inc). Data was collected using SerialEM (Mastronarde, 2005) at a nominal magnification of 25,000x with a pixel size of 1.479 Å/px, dose rate of approximately 7 e^-/px/s with 0.2 s frames over 10 s, and a defocus range between -1.3 and -2. A total of 651, 645, and 509 images were collected for Glyco-DIBMA, SMALP 200, and CyclAPol C_8-C_0-50, respectively. Bsoft 2.2.0 (Heymann and Belnap, 2007) was used for unpacking the image stacks. Image processing was performed using cisTEM v1.0.0. (Grant et al., 2018). 37,902, 237,492, and 158,613 particles were picked from the micrographs after CTF estimation (Rohou and Grigorieff, 2015) for Glyco-DIBMA, SMALP 200, and CyclAPol C_8-C_0-50, respectively, using a maximum radius of 60 Å and a characteristic radius of 40 Å with a threshold of 5. Particles were extracted with a box size of 168 px (~250 Å) and analyzed using 2D classification.

Cryo-EM Grid Preparation and Data Collection

3 µL of purified MscS between 0.1 and 0.7 mg/mL was applied to a glow discharged Quantifoil R 1.2/1.3 + 2 nm C 400 Cu mesh grid (EMS), a holey grid with a thin 2 nm continuous carbon film. The grids were blotted for 6 s at 4 °C and 95% humidity, and plunge-frozen into liquid ethane using a Leica EM GP2 (Leica) and stored in liquid nitrogen. For the Glyco-DIBMA extracted MscS a double sample application was performed where 3 µL of sample was applied, blotted by hand using Whatman Grade 2 filter paper, then 3 µL was re-applied and blotted using the Leica EM GP2. The grids were screened on an FEI Tecnai T20 TEM before data collection. Cryo-EM datasets were acquired with SerialEM (Mastronarde, 2005) using a Titan Krios (FEI, now ThermoFisher Scientific) operated at 300 kV and equipped with an energy filter and K3 camera (Gatan Inc.). Movies of 50-60 frames were collected with a total dose of 50 $e^-/Å^2$ at a nominal magnification of 105,000x corresponding to a physical pixel size of 0.83 or 0.85 Å/px at a dose

rate of 9-15 e^-/px/s and a defocus range of -0.8 to -1.8 µm. Specific collection parameters for each dataset can be found in Supplemental Table 1.

Cryo-EM Data Processing

The specific workflows for image processing are illustrated in Supplemental Figures 5-9. All processing was performed within cryoSPARC v3.3.250 (Punjani et al., 2017). Movies were processed with patch motion correction (Zheng et al., 2017) and patch CTF estimation (Rohou and Grigorieff, 2015). Blob picker was used for the majority of particle picking and particles were extracted with a box size of 320-360 px (~300 Å) and subjected to 2D classification to remove junk particles. Selected particles were used for ab-initio reconstruction, heterogeneous refinement, and non-uniform refinement using no symmetry (C1) as well as 7-fold symmetry (C7) (Punjani et al., 2020). The local resolution was estimated, and the maps were filtered accordingly. Additional CTF refinements and local motion correction did not improve resolution, most likely because the 2 nm carbon layer support reduces beam induced motion (Campbell et al., 2012).

Model Building and Refinement

For the MscS atomic model, PDB 7ONL (Flegler et al., 2021) was rigid-body fitted into the to the local resolution filtered map using UCSF ChimeraX v.1.6.1 (Pettersen et al., 2021). The model was then manually rebuilt in COOT v.0.8.9.2 (Emsley et al., 2010) using the same map, which was generated from non-uniform refinement with C7 applied. Iterative rounds of manual refinement in COOT and real-space refinement in Phenix v.1.20.1-4487 (Liebschner et al., 2019) were performed. The quality of the model and fit to the density was assessed using MolProbity (Williams et al., 2018) and Phenix. All structural figures were prepared using UCSF ChimeraX v.1.6.1 (Pettersen et al., 2021). Cryo-EM map and model analysis values are listed in Supplemental Table 2. PDBs have been made available together with the cryo-EM maps with the following EMD/PDB IDs: XXXX/xxxx for the MscS/Glyco-DIBMA (C7), XXXX/xxxx for the MscS/Glyco-DIBMA (C1), XXXX for the MscS/SMALP 200 (C7), and XXXX for the MscS/CyclAPol C_8-C_0-50 (C7). Movies as well as particle stacks will be uploaded to EMPIAR (Iudin et al., 2022).

Lipid Mass Spectrometry

The remaining purified MscS sample in Glyco-DIBMA from purification #2 was used for Mass Spectrometry Lipid Analysis along with a control sample of purified *E. coli* inner membranes (see *MscS Expression and Inner Membrane Isolation)*. 1 µL of sample pellet was scraped and plated directly to a steel re-usable MALDI plate. 1 µL of 70% citric acid extraction buffer was spotted on top of the plated

sample. The steel MALDI plate was added to the chamber with water on the bottom and placed in a 110ºC oven for 30 minutes. After, the plate was rinsed with water and air dried, 1 µL of Norharmane matrix was spotted on each sample. A Bruker Matrix-Assisted Laser Desorption/Ionization trapped ion mobility spectrometry Time-of-Flight Mass Spectrometry MALDI (tims TOF) MS was used for FLAT (direct biomass MS for visualization of lipid A and phospholipids) and direct analysis. This MALDI (tims TOF) MS is equipped with a dual ESI/MALDI source with a SmartBeam3D 10 kHz frequency tripled Nd:YAG laser (355 nm); the system was operated in "qTOF" mode (TIMS deactivated) for these experiments. Ion transfer tuning was used with the following parameters: funnel1 RF, 440.0 Vpp; funnel2 RF,490.0 Vpp; multipole RF, 490.0 Vpp; CID energy, 0.0 eV; and deflection delta, -60.0 V. Quadrupole was used with the following values for MS mode: ion energy, 4.0 eV. The m/z scan range for MS is set to 1000 to 3000. Collision cell activation of ions used the following values for MS mode: collision energy, 9.0 eV; collision RF, 3900.0 Vpp. In the MS/MS mode, the precursor ion was chosen by typing the targeted m/z value including two digits to the right of the decimal point. Typical isolation width and collision energy were set to 4−6 m/z and 100−110 eV, respectively. FocusPre TOF used the following values for transfer time, 110.0 µs, and prepulsestorage, 9.0 µs. Agilent ESI tune mix was used to perform calibration of the m/z scale. MALDI parameters in qTOF were optimized to maximize intensity by tuning ion optics, laser intensity, and laser focus. All spectra were collected at a 104 µm laser diameter with beam scan on using 800 laser shots per spot and 70 and 80% laser power, respectively. MS data were collected in negative ion mode. In all cases, 10 mg/mL of norharmane (NRM) in 1:2 MeOH/CHCl3 [v:v] was used for lipid detection. All MALDI (tims TOF) MS were visualized using mMass (Ver 5.5.0). Peak picking was conducted in mMass using the following parameters: S/N threshold: 3.0; relative intensity threshold: 5.0%; picking height: 50; apply baseline and smoothing.

Mutagenesis and Patch Clamp Electrophysiology

Point mutations were introduced to the MscS plasmid at positions R59, K60, D67, and R88 using the Q5 site-directed mutagenesis kit (NEB). Giant spheroplasts were generated as described previously (Martinac et al., 1987). In short, cells were grown in LB to turbidity and then sub-cultured 1:9 into MLB (250 mOsm) and grown for 1.5 h in the presence of 0.06 mg/ml cephalexin, which prevents cell septation, before inducing with 1 mM IPTG for the final 30 min. The resulting filaments were transferred into 1 M sucrose with 1.8 mg/ml BSA buffer and treated with 0.17 mg/ml lysozyme in the presence of 4 mM EDTA, which degrades the peptidoglycan layer and causes the filaments to collapse into giant spheres. The reaction was stopped with 5 mM $MgCl_2$. The giant spheroplasts were isolated via sedimentation through a one-step 1.2 M sucrose gradient at 2,000 rpm using Eppendorf Rotor A-4-81 for 5 min at 4ºC.

Patch-clamp traces were recorded from giant bacterial cell spheroplasts. Population channel recordings were conducted at ±30 mV (pipette) on excised inside-out patches in symmetric buffer containing 400 mM sucrose, 200 mM KCl, 50 mM $MgCl_2$, 5 mM $CaCl_2$, and 5 mM HEPES at pH 7.4. Membrane patches were obtained using borosilicate glass pipettes (Drummond) and recorded on an Axopatch 200B amplifier (Molecular Devices). Negative pressure stimuli were applied using a high-speed pressure clamp apparatus (HSPC-1; ALA Scientific) programmed using the Clampex software (Molecular Devices). Pressure and voltage protocol programming and data acquisition were performed with the PClamp 10 suite (Axon Instruments). The patch responses were first recorded at +30 mV (pipette) with symmetric 1-s pressure ramps to determine the activation thresholds, midpoints, and saturation level for the MscS population in both MJF465 and PB113 where MscL is also present for comparison. PB113 (ΔmscS ΔmscK) is derived from the MJF429 strain (Levina et al., 1999) with the additional ΔrecA (Li et al., 2002) and was provided by Paul Blount (University of Texas at Dallas, Richardson, TX, USA). The standard pipettes were pulled to bubble number of 5.3–5.5. Based on the previously reported tension midpoints for both MscS and MscL (Belyy et al., 2010b; Moe and Blount, 2005; Nomura et al., 2012; Sukharev, 2002; Sukharev et al., 1999), the radius of a stretched hemispherical patch was estimated as 1.4 ± 0.1 µm. To observe the inactivation of MscS, a pulse-step-pulse was used (Akitake et al., 2005; Kamaraju et al., 2011): the full population of channels was opened with a saturating test pulse and then held at the midpoint tension for MscS for 10 s followed by three test pulses with zero pressure steps in between. The rate of recovery (τ) was determined from fitting the recovery pulses to a monoexponential function. Percent inactivation was taken from one minus the first test pulse, normalized to the initial pulse.

Results

E. coli MscS polymer extraction and characterization

MscS is a model system for MSCs that are gated directly by tension in the surrounding bilayer, and, as such, understanding the role of lipids is essential. The use of polymer extraction for structural studies ideally preserves a more native lipid environment with less disruption than traditional detergent solubilization which delipidate proteins (Supplemental Figure 1). Three polymers were attempted in parallel under similar extraction conditions: SMALP 200, CyclAPol C_8-C_0-50 (now known as Ultrasolute Amphipol 18), and Glyco-DIBMA. SMALP 200 was the original polymer that was shown to work for direct extraction and structural characterization, CyclAPols overcame many of the limitations associated with the SMALP chemistry including restrictions on pH and divalent cations, and Glyco-DIBMA is a novel polymer that has not been used previously for cryo-EM. For all three polymers the extraction was less efficient than detergent solubilization and proved to be most effective at room temperature rather than

the typical 4°C. The concentrations of each polymer were chosen to be at the lowest range given by the manufacturer. A larger range of concentrations from 0.1% to 2% were initially tested for SMALP 200, but decreasing the polymer concentration was detrimental to extraction efficiency and increasing it did not improve extraction in a linear fashion based on SDS-PAGE and Western Blots comparing the soluble and insoluble fractions after ultracentrifugation. As polymers have been previously shown to interact with membrane proteins the lowest effective range was chosen. Membrane concentrations from 10 mg/mL to 30 mg/mL were tested, and we found that increasing the dilution only marginally improved the extraction efficiency. Room temperature solubilization rather than at 4°C greatly improved extraction, likely due to the phase of the lipids at this temperature (Huang and Li, 1999). Higher temperatures have been used previously and proved effective (Kopf et al., 2020) but were not attempted in this comparison. Even when allowed to extract overnight at 4°C the extraction was lower than at room temperature for 2 hours. Room temperature extraction for longer than 2 hours was not tested but may prove effective provided that the protein is stable. The buffers for SMALP 200 and CyclAPol C_8-C_0-50 were based on previous publications (Higgins et al., 2021). HEPES was chosen for Glyco-DIBMA since the polymer is commercially available in that buffer. Negative Staining Electron Microscopy (EM) is shown for each of these polymers alone in the appropriate buffers at the concentrations used for the extractions in Supplemental Figure 10. At medium magnification there is already a macroscopic pattern visible for each polymer, and at high magnification clusters of varying sizes are observed. Polymer extracted MscS was purified by a cobalt affinity column and analyzed by SDS-PAGE, Western Blot, and BN-PAGE (Supplemental Figures 2-4A-C). SDS-PAGE and Western Blot confirmed the identity and purity of the sample. The BN-PAGE was inconclusive with the majority of the protein remaining in the well rather than running according to the size of the heptamer. Despite this, the sample looked promising albeit heterogenous using Negative Staining EM with some isolated particles and clear MscS top views resembling rings even though an approximately 30 times higher protein concentration was necessary compared to detergent solubilized MscS or MscS in mixed micelles (Supplemental Figures 2-4D). The CyclAPol C_8-C_0-50 Negative Staining EM micrographs were the most similar in appearance to detergent with distinct particles and only some clusters/aggregation (Supplemental Figure 3D). SMALP 200 was noticeably more aggregated but still had distinct particles identifiable as MscS (Supplemental Figure 4D). Glyco-DIBMA was extremely heterogeneous with entire membrane patches interspersed with the single particles (Supplemental Figure 2D). For all three polymers the Negative Staining EM data collection and processing resulted in MscS-like 2D classes (Supplemental Figures 2-4E), and we proceeded to cryo-EM.

Cryo-EM of E. coli MscS in native nanodiscs

The initial structural attempts to solve MscS in a native nanodisc with both SMALP 200 and CyclAPol C_8-C_0-50 were only partially successful under the purification conditions that were tested, resulting in side view 2D class averages with a blurry TM region and 3D maps with unresolved TMs. However, using the Glyco-DIBMA polymer to form native nanodiscs yielded a complete 3D reconstruction (Figure 1). A selection of the 2D class averages used for the 3D reconstruction are shown in Figure 1A showing clear features in the TM region in typical side view 2D class averages. These features are lacking in the blurry TM region from the SMALP 200 and CyclAPol extracted MscS averages (Supplemental Figure 11). The overall map resolution is 2.99 Å with the highest resolution in the cytoplasmic domain estimated to reach 2.6 Å (Figure 1B). Side chain densities for a helix and beta sheet are shown in Supplemental Figure 12. At this resolution the protein was modelled from residue 17 to 281 out of the 287 total residues (Figure 1C). The structure is non-conductive with the TM helices tilted inward at the top and splayed away from the pore lining helix. The 2D class averages that contributed to this 3D reconstruction comprised the isolated particles rather than those found in the larger lipid patches/small vesicles.

An additional class (Class 2, Supplemental Figure 6E,D) resulting from averaging particles from small vesicles or membrane patches was observed during processing, but so far, no transmembrane domain could be resolved (Supplemental Figure 13). These side views have clear density for the lipid bilayer extending to the edge of the box in some cases, in addition to a recognizable cytoplasmic domain. This liposome-like class has unique top view 2D class averages as well, appearing tight and sharply star shaped without an opening for the pore. Similar top view 2D class averages have not been observed in detergent solubilized or mixed micelle MscS samples but are also seen for our SMALP 200 and CyclAPol C_8-C_0-50 solubilized samples (Supplemental Figures 7-9) even though the reconstructions of MscS in these polymers resulted in unresolved TM's.

Densities unaccounted for by the modelled protein were examined and some of them were modelled as lipids. Both POPE and POPG were considered, but due to the higher prevalence of POPE in the *E. coli* inner membrane and lacking a significant increase in POPG in the extracted sample by lipidomics (see below), POPE is currently placed inside these extra densities. These densities, revealing not only the lipid tails but also the headgroups, are shown in Figure 2. Lipid 1 (Figure 2D) is oriented parallel to the bilayer outer leaflet between TM2s of neighboring chains. Lipids 2-4 (Figure 2E-G) are oriented perpendicular to the bilayer inner leaflet between the loops connecting TM1 and TM2 of neighboring chains. The extraction ability of the Glyco-DIBMA polymer is clear, retaining lipid patches of varying sizes surrounding the protein. The density of these native nanodiscs surrounding the Glyco-DIBMA extracted

MscS is tighter than is seen in a pure detergent micelle. This, along with other remaining unmodelled densities, are shown in Supplemental Figure 14.

Mass-spectrometry of co-purified lipids and comparison with the inner membrane composition

The results of MALDI-TOF mass spectroscopic analysis of lipids copurified with MscS in the course of extraction with Glyco-DIBMA and enrichment on a cobalt affinity column are shown in Figure 3A. Figure 3B provides a comparison with the lipid composition in the inner membrane fraction isolated from the same expresser strain using a sucrose gradient. In the positive ion-detection mode, we see regularly spaced peaks reflecting the presence of polymers with different degrees of conjugation. In the negative-ion detection mode, we could detect the four most abundant PE species with one or two unsaturated bonds, two prevalent PG species, and one cardiolipin (CL). The fraction had a small admixture of Lipid A that metabolically passes through the inner membrane on the way to the outer membrane. The total inner membrane fraction has essentially identical composition (Figure 3C), with an extra species of CL and a slightly smaller fraction of PE 33:1. We cannot conclude any substantial enrichment or depletion of lipids copurified with MscS which could be because whole membrane patches and small vesicles have been purified as well as single channel particles.

Lipid coordination in the crevices by specific residues and functional effects of mutations in situ

The protein-lipid contacts are stabilized by the electrostatic interactions of the lipid headgroups with charged residues in the gaps and crevices, most noticeably R88 for Lipid 1, and R59, K60 and D67 for Lipids 2-4. There are also multiple nonpolar contacts between hydrophobic residues and the aliphatic chains. A full list of nearby residues is given in Supplemental Table 3. To investigate how these interactions affect the function of MscS, we made several mutations and conducted functional tests on giant spheroplasts using patch-clamp (Figure 4). Lipid 1 clinging to R88 in the gap between the periplasmic ends of the TM1 helices has been the most readily observed in prior structures. Although the densities of aliphatic chains are clear, the nature of the headgroup cannot be easily identified. However, the interactions of the guanidine group of R88 with the phosphate would stabilize almost any type of lipid in this place. We asked what would happen if this interaction was weakened by either a neutralizing mutation or charge reversal. Figure 4A-C shows three traces recorded on WT MscS, R88Q and R88E illustrating the depth of inactivation and the kinetics of recovery. The neutralizing mutation R88Q did not produce any statistical difference from WT. The charge-reversal R88E increased the depth of inactivation and considerably slowed down the recovery. The small-sidechain substitution R88A had a subtle intermediate effect (see Supplemental Table 4 for statistics). We cannot exclude the possibility that the carboxyl of R88E may interact with the amino group of PE thus stabilizing the lipid in a similar

conformation. We may also assume that the charge-reversal mutation stabilizes a different conformation of periplasmic TM1 helices leading to slower recovery.

The polar parts of Lipid 2 and Lipid 3 predominantly interact with R59's sidechain, with some contribution from K60. Lipid 4 interacts with the nearby D67. We conducted recordings with the inactivation-recovery protocol after introducing individual alanine substitutions for R59, D67 and K60. Figure 4D-F shows the results, and the summary of extracted parameters is presented in Supplemental Table 4. Our observations indicate that R59A exhibits minimal inactivation, especially at +30 mV in the pipette. The traces show no sign of recovery, suggesting that this mutant greatly resists inactivation under these conditions. Similarly, K60A shows only slight inactivation. Conversely, D67A inactivates completely, and recovers very quickly when the pipette pressure drops to zero. Based on our results, we hypothesize that the lipid-intercalated state of the TM2-TM3 crevice, stabilized primarily by R59 interacting with the lipid phosphate and D67 interacting with the amino group of PE, corresponds to the inactivated state of the channel. The intercalation is 'invited' by R59, and when the lipid gets into the crevice, it is likely additionally stabilized by D67. R59A shows minimal inactivation. It is important to note that in the D67A mutant, R59 is in place and electrostatically unopposed due to the absence of the nearby D67 chain. Therefore, D67A is more willing to inactivate, but the lack of a counterpart for interaction with the amino group of PE (Lipid 4) may make PE leave the crevice more quickly. The lipid expulsion from the crevices might be cooperative, which is why the departure of Lipid 4 may promote the exit of other lipids, resulting in the compaction of the transmembrane domain and the re-establishment of the functionally predicted TM2-TM3 contact (Belyy et al., 2010a).

Structure comparison of E. coli MscS in different environments

Structurally speaking the Glyco-DIBMA polymer extracted MscS structure is the most similar to PDB 6PWN (Reddy et al., 2019) (Figure 5A), with modelled lipids very similar to PDB 6LRD (Rasmussen et al., 2019). Both of these structures are in synthetic MSP nanodiscs with a mixture of POPC and POPG for the former and azolectin for the latter. They closely resemble PDB 6YVK (Zhang et al., 2021) which is a third example of a synthetic nanodisc structure in POPC. These structures are all similar to MscS reconstituted into peptidiscs (6UZH (Angiulli et al., 2020)), albeit without any resolved lipids, which the authors attribute to the peptidiscs inability to retain loosely associated lipids or lipids that require a true bilayer. Another way to ensure lipidation of membrane proteins is to provide lipids in the form of mixed micelles such as in PDB 7OO6 (Flegler et al., 2021) (Figure 5B) which is also structurally close to the Glyco-DIBMA polymer extracted structure, MSP nanodisc structures, and peptidisc structure. When comparing these with the original crystal structure 2OAU (Bass et al., 2002), they all have a similar

architecture with inward tilted TM1-2 helices splayed away from the pore lining helix (Supplemental Figure 15). The biggest differences are in the loops connecting TM1 to TM2 and the overall angle of the TM1-TM2 helical bundle with the Glyco-DIBMA extracted structure slightly more upright when compared to the plane of the bilayer. The N-terminal residues are poorly resolved until residue 17 indicating that they are flexible and disordered in contrast to the structured helix seen in 6PWN (Reddy et al., 2019) and 6YVK (Zhang et al., 2021). Glyco-DIBMA extracted MscS is dramatically different in the TM helix angles when compared to the detergent solubilized structures 7OO0 (Flegler et al., 2021) and 7ONJ (Flegler et al., 2021), the nanodisc structures with short chain lipids 6YVL (Zhang et al., 2021) and 8DDJ (Park et al., 2023), and the crystal structure of the A106V mutant 2VV5 (Wang et al., 2008) (Supplemental Figure 15). These have been previously proposed as the open state of the channel with the TM3a helix containing the gate becoming more upright as well as the rearrangement of the TM1-TM2 helical bundle. The nanodisc structure with full-length lipids that were then removed using ß-cyclodextrin in PDB 6VYM (Zhang et al., 2021) is interesting in that TM3a still aligns with the Glyco-DIBMA extracted structure making it non-conductive, but there is a huge change in the TM1-TM2 helical bundle angle as the lipids are pulled away (Supplemental Figure 15). The RMSD comparison of these structures was calculated by aligning the cytoplasmic domains and calculating the average distances for the entire chain using Visual Molecular Dynamics (VMD) (Humphrey et al., 1996).

Lipid 1 is in a similar location as previously reported lipids in 6PWN (Reddy et al., 2019), 6LRD (Rasmussen et al., 2019), and 6YVK (Zhang et al., 2021). 6LRD (Rasmussen et al., 2019) also has two out of the three lipids that stack perpendicular to the plane of the bilayer in the lower crevices between two chains of the neighboring TM1-TM2 helical bundles. 6PWN (Reddy et al., 2019) has additionally modelled 7 single lipid tails without density for lipid headgroups in the pore of the protein along TM3a above the gate. We also have disordered density in these regions but could not model them as lipids as they are along the symmetry axis of the protein and lacking well resolved headgroups. There is a possibility that they are intermediates for lipid synthesis or lipid breakdown products. The locations of modelled detergent on the periphery of the protein, both DDM (7OO0 (Flegler et al., 2021)) and LMNG (7ONJ (Flegler et al., 2021)), align quite well with the locations of our modelled lipids. These have also extra densities within the pore of the protein with two rings of detergent molecules oriented tail to tail along TM3a modelled in. The mixed micelle structure 7OO6 (Flegler et al., 2021) has modelled a lipid in the position 1 and 7 detergent molecules at the top ring of the pore.

Discussion

The results presented above depict the structure of MscS solved in a detergent-free environment. It represents the first use of the novel Glyco-DIBMA polymer (Danielczak et al., 2022) for solving the

structure of a membrane protein. The polymer was expected to 'cut' the protein out of its native membrane together with some annular lipids, which could be resolved in their native positions without causing the complete de-lipidation of the transmembrane domain, thus preserving its native conformation. In support of these hypotheses, we observe a variety of 2D class averages with different sizes of a lipid patch around the protein's hydrophobic rim (Supplemental Figure 13). The polymer is capable of excising large patches of native membrane with incorporated proteins and the resulting heterogeneous sample can still be used for high-resolution single particle cryo-EM. It is unsurprising therefore that the comparison of lipidomic data obtained on purified MscS complexes and intact inner membranes (Figure 3) suggests no significant enrichment or depletion of specific lipids that co-purify with the MscS complex when compared to the rest of the inner membrane. This heterogeneity could provide opportunities to obtain structural information from large membrane patches and may be used in the future to provide insights into bilayer position and thickness. These large membrane patches were most readily observed when using Glyco-DIBMA which may indicate that it acts less aggressively in the membrane than other polymers. The other polymers may interact directly with the hydrophobic TM domains of the protein to disrupt the structure, resulting in the unresolved domains and blurry 2D class averages. Another explanation could be that the binding of the other polymers to the lipid-protein complex is not stable enough and, as the buffers are lacking additional lipids and polymers to exchange with, they dissociate from the protein. If the polymers and lipids dissociate from the TM region those domains will become unstable and may start to disintegrate. It is important to consider however that these polymers were also tested in the presence of glycerol at a slightly different pH using Tris/HCl buffer instead of HEPES and may work well for structural studies under different conditions. The unique top views observed in all the polymer extracted MscS samples should likewise be investigated further.

The conformation of the channel backbone is almost identical to previous structures solved in synthetic nanodiscs formed of full-length lipids (6PWN) with minor deviations (0.9 Å RMSD) in the two most flexible regions, the unsupported periplasmic ends of TM1 helices and the cytoplasmic TM1-TM2 loops. MscS solved in mixed lipid-detergent micelles (7OO6) shows a slightly higher RMSD due to torsional displacement of TM1-TM2 pairs, possibly due to altered lateral pressure exerted by the lipid coat. The RMSDs from semi-open structures obtained in DDM or short-chain lipid nanodiscs are much larger (~8-10 Å with some regions over 23 Å). Based on all criteria, our structure belongs to the original 2OAU class of non-conductive structures with peripheral helices splayed away from the pore forming TM3a barrel. The close spatial alignments of many similar splayed structures obtained under different conditions indicate a highly stable non-conductive protein conformation.

The splayed conformations of the 2OAU class have been interpreted as the closed state in several studies (Flegler et al., 2021; Rasmussen et al., 2019; Reddy et al., 2019; Zhang et al., 2021). Multiple attempts to open this structure in Molecular Dynamics simulations under applied tension did not result in a fully conductive state (Park et al., 2023; Sotomayor and Schulten, 2004). The attempts to obtain an open state in experiments with nanodisc-reconstituted MscS exposed to cyclodextrins (Zhang et al., 2021) resulted in structures that do not seem to satisfy the conductive properties. Notably, none of that work considered the stable splayed conformation as the inactivated state of the channel. To close this information gap, we emphasize that MscS is a three-state channel that is sensitive to relatively small tensions, i.e., the reduction of lateral pressure from lipids. It inactivates *in situ* when subjected to near-threshold tensions of 5-6 mN (for tens of seconds). Removing the bulk of the bilayer during detergent or polymer extraction likely produces the same effect. Our functional experiments, informed by the structural data shown above, precisely support this scenario and assign the 2OAU class of structures to the inactivated state. We consider the possibility that this stable non-conductive and tension insensitive state is a preferred 'default' state of the channel as soon as you disrupt the native bilayer even when lipids are retained. Upon complete detergent solubilization the Laplace pressure is further reduced, resulting in the expanded conformation. A return of the population to the closed 'ready-to-open' state may require an intact bilayer and the metabolic energy of the cell.

The protein extraction using Glyco-DIBMA allowed us to visualize co-purified native lipids, model the conformations of aliphatic chains, and reliably determine the positions of the lipid headgroups. We have identified the polar and non-polar interactions that stabilize these lipids non-bilayer positions (Supplemental Table 3). Our data confirm the presence of Lipid 1 clinging to R88 (Rasmussen et al., 2019; Reddy et al., 2019) and demonstrate better-resolved densities for Lipids 2-4 on the cytoplasmic side. The neutralizing substitutions for R88 did not produce a strong effect apart from a slight increase in activating tension (Supplemental Table 4). The charge-reversal R88E mutation increased activation tension and moderately slowed down the process of recovery from inactivation. We do not know how the mutations would impact the structure, which features significant gaps in the barrel lining between the periplasmic ends of TM1 helices when R88 is absent or replaced by glutamine or glutamate. The mutations may not prevent the intercalation of a lipid between the helices, as is seen for WT. The phenotypes of R88 substitutions are mild, and the role of this residue, which is not highly conserved, still needs to be elucidated.

Lipids 2-4 are located on the cytoplasmic side and wedge between the TM1-TM2 helical pairs. The peripheral residues of R59, K60, and D67, electrostatically stabilizing these lipids in 'non-bilayer'

(parallel to the membrane plane) conformations between the helices, have been mutated and showed distinct gating phenotypes. The strongest non-inactivating phenotype was produced by the R59A substitution, which eliminated the charge stabilizing Lipid 2 (Figure 4). The K60A mutation removed interactions with Lipid 3 and produced a qualitatively similar phenotype. In contrast, eliminating D67, which balances the charge in the vicinity of R59 and interacts with amino groups of Lipid 2 (and possibly Lipid 4), produces an opposite strongly inactivating phenotype. Since eliminating the stabilizing electrostatic interactions with positive sidechains prevents inactivation, we conclude that the revealed cryo-EM structure represents the inactivated state. We believe the Lipids 2-4 serve as the 'filler' that separates the lipid-facing TM1-TM2 pairs of helices from the TM3 barrel, thus interrupting the force transmission route from the lipid to the gate.

The next question is what mechanism removes these lipids from the gaps to restore the previously predicted compact closed conformation and re-establish the TM2-TM3 hydrophobic contact (Belyy et al., 2010a). It seems unlikely that membrane tension can 'yank' these sequestered lipids out of the crevices (Pliotas et al., 2015), and propose that the metabolically generated positive lateral pressure of lipids would provide the major restoring force to squeeze the lipids out and compact the TM barrel. The experimentally estimated area expansion associated with inactivation (~8 nm^2) is consistent with the transition from the modeled compact state (Anishkin et al., 2008; Belyy et al., 2010a) to the splayed conformation revealed by the structure (Figure 6). At this moment, we do not discuss the compact and open-state models because they are currently being refined and will be reported later. The kinetic scheme in Figure 6 shows the place for the new MscS-lipid complex that, according to patch-clamp data (Figure 4), is a result of the slow (~10 s) inactivation transition under moderate (~6 mN/m) tension. The kinetic scheme emphasizes the qualitative difference between the two expansion pathways, a steeply tension-dependent and fast opening-closing pathway and a very slow inactivation-recovery pathway. The opening and closing transitions were found to be essentially frictionless, non-perturbing, and non-dissipative (Çetiner et al., 2023), indicating that lipid re-arrangement is not possible. The slow inactivation and recovery transitions on the other hand are strongly voltage-dependent, which suggests that inactivation is specifically associated with the rearrangement of the protein-lipid boundary (Britt et al., 2024).

In conclusion, we show that the MscS structure solved in the presence of the amphipathic Glyco-DIBMA polymer is a stable conformation with inward tilted TM helices splayed away from the gate very similar to the previously solved structures in full-length synthetic lipid nanodiscs or mixed micelles. A critical advantage of polymer solubilization is that we can confidently assign the proposed densities to lipids as there is no detergent present in our sample, in contrast to all prior structures of MscS. These well-defined

conformations of lipids between the adjacent TM1 helices and between TM2 and TM3 helices uncouple the gate from the peripheral tension-sensing helices and thus interrupt the tension transmission route, representing a novel lipid-mediated mechanism of channel inactivation. Specific charged residues stabilize these lipid positions, and functional experiments have demonstrated that eliminating these positive charges largely precluded inactivation, whereas eliminating a balancing negative charge in that vicinity increased the tendency toward inactivation. The use of this polymer increased the predictive power of our cryo-EM structure, which allowed us to associate the solved conformation with the inactivated state of the multi-state mechanosensitive channel MscS.

Acknowledgements

We thank Joshua Zimmerberg and Jennifer Peterson for access to the Tecnai T20 electron microscope and AJ Morton, Zabrina Lang, and Rick K. Huang for the support on the Krios G1, Wyatt Peele and Mario Borgnia for the support on the Krios G4. We are grateful to Samantha Miller for providing the MJF465 strain, Paul Blount for providing the PB113 strain, Manuela Zoonens for providing the CyclAPol C_8-C_0-50 polymer, Gerald Kidd for assistance in membrane isolation, and Alex Sodt and Louis Tung Faat Lai for valuable discussions. The research was supported by the Division of Intramural Research of the *Eunice Kennedy Shriver* National Institute of Child Health and Human Development, NIH (grant NICHD intramural projects Z1A HD008998 to DM). This work was supported by NIH R01-AI135015 to SS. This material is based upon work supported by the National Science Foundation Graduate Research Fellowship Program to EM under Grant No. DGE 1840340. Any opinions, findings, and conclusions or recommendations expressed in this material are those of the author(s) and do not necessarily reflect the views of the National Science Foundation. This work utilized the computational resources of the NIH HPC Biowulf cluster. (http://hpc.nih.gov). Molecular graphics and analyses performed with UCSF ChimeraX, developed by the Resource for Biocomputing, Visualization, and Informatics at UCSF, with support from NIH R01-GM129325 and the Office of Cyber Infrastructure and Computational Biology, NIAID. Supplemental Figure 1 was created with BioRender.com.

Author Contributions

EM: membrane isolation, purification, biochemistry (SDS, Western, BN), negative stain microscopy and data collection, grid freezing, cryo data processing, model building and refinement, mutagenesis, patch clamp, figure making, writing, funding

MB: membrane isolation, patch clamp, figure making, writing

FZ: help and support with biochemistry, cryo grid screening, Krios data collection

HY: lipid mass spec

AA: molecular dynamics simulations, writing

RE: lipid mass spec

SS: membrane isolation, sample prep for mass spec, data interpretation, writing, supervision and training, funding

DM: model building, writing, supervision and training, funding

Author details (Name, address, phone, e-mail, ORCID IDs)

Elissa Moller; 29 Lincoln Dr, Bethesda, MD 20982; elissa.moller@nih.gov, emoller@umd.edu; ORCID: 0000-0002-2467-0709

Madolyn Britt; Biology-Psychology Bldg, 4094 Campus Drive, UMD, College Park, MD 20842; mbritt@umd.edu
Fei Zhou; 29 Lincoln Dr, Bethesda, MD 20982; fei.zhou@nih.gov
Hyojik Yang; 650 W. Baltimore St. Room 8203 Baltimore, MD 21201
Andriy Anishkin; Biology-Psychology Bldg, 4094 Campus Drive, UMD, College Park, MD 20842
Robert Ernst; 650 W. Baltimore St. Room 8203 Baltimore, MD 21201; rkernst@umaryland.edu
Sergei Sukharev; Biology-Psychology Bldg, 4094 Campus Drive, UMD, College Park, MD 20842; sukharev@umd.edu; ORCID: 0000-0002-4807-9665
Doreen Matthies; 29 Lincoln Dr, Bethesda, MD 20982; +1-202-417-4982; doreen.matthies@nih.gov; ORCID: 0000-0001-9221-4484

References

Akitake, B., A. Anishkin, N. Liu, and S. Sukharev. 2007. Straightening and sequential buckling of the pore-lining helices define the gating cycle of MscS. *Nat Struct Mol Biol*. 14:1141-1149.

Akitake, B., A. Anishkin, and S. Sukharev. 2005. The "Dashpot" Mechanism of Stretch-dependent Gating in MscS. *The Journal of general physiology*. 125:143-154.

Angiulli, G., H.S. Dhupar, H. Suzuki, I.S. Wason, F. Duong Van Hoa, and T. Walz. 2020. New approach for membrane protein reconstitution into peptidiscs and basis for their adaptability to different proteins. *eLife*. 9:e53530.

Anishkin, A., B. Akitake, and S. Sukharev. 2008. Characterization of the resting MscS: modeling and analysis of the closed bacterial mechanosensitive channel of small conductance. *Biophys J*. 94:1252-1266.

Bass, R.B., P. Strop, M. Barclay, and D.C. Rees. 2002. Crystal structure of Escherichia coli MscS, a voltage-modulated and mechanosensitive channel. *Science*. 298:1582-1587.

Belyy, V., A. Anishkin, K. Kamaraju, N. Liu, and S. Sukharev. 2010a. The tension-transmitting 'clutch' in the mechanosensitive channel MscS. *Nat.Struct.Mol.Biol.* 17:451-458.

Belyy, V., K. Kamaraju, B. Akitake, A. Anishkin, and S. Sukharev. 2010b. Adaptive behavior of bacterial mechanosensitive channels is coupled to membrane mechanics. *J Gen Physiol*. 135:641-652.

Boer, M., A. Anishkin, and S. Sukharev. 2011. Adaptive MscS gating in the osmotic permeability response in E. coli: the question of time. *Biochemistry*. 50:4087-4096.

Britt, M., E. Moller, J. Maramba, A. Anishkin, and S. Sukharev. 2024. MscS inactivation and recovery are slow voltage-dependent processes sensitive to interactions with lipids. *Biophysical Journal*. 123:195-209.

Campbell, M.G., A. Cheng, A.F. Brilot, A. Moeller, D. Lyumkis, D. Veesler, J. Pan, S.C. Harrison, C.S. Potter, B. Carragher, and N. Grigorieff. 2012. Movies of ice-embedded particles enhance resolution in electron cryo-microscopy. *Structure*. 20:1823-1828.

Çetiner, U., A. Anishkin, and S. Sukharev. 2018. Spatiotemporal relationships defining the adaptive gating of the bacterial mechanosensitive channel MscS. *Eur Biophys J*. 47:663-677.

Çetiner, U., O. Raz, M. Britt, and S. Sukharev. 2023. Dissipation during the Gating Cycle of the Bacterial Mechanosensitive Ion Channel Approaches the Landauer Limit. *Entropy*. 25:779.

Danielczak, B., M. Rasche, J. Lenz, E. Pérez Patallo, S. Weyrauch, F. Mahler, M.T. Agbadaola, A. Meister, J.O. Babalola, C. Vargas, C. Kolar, and S. Keller. 2022. A bioinspired glycopolymer for capturing membrane proteins in native-like lipid-bilayer nanodiscs. *Nanoscale*. 14:1855-1867.

Emsley, P., B. Lohkamp, W.G. Scott, and K. Cowtan. 2010. Features and development of Coot. *Acta Crystallogr D Biol Crystallogr*. 66:486-501.

Flegler, V.J., A. Rasmussen, K. Borbil, L. Boten, H.-A. Chen, H. Deinlein, J. Halang, K. Hellmanzik, J. Löffler, V. Schmidt, C. Makbul, C. Kraft, R. Hedrich, T. Rasmussen, and B. Böttcher. 2021. Mechanosensitive channel gating by delipidation. *Proceedings of the National Academy of Sciences*. 118:e2107095118.

Grant, T., A. Rohou, and N. Grigorieff. 2018. cisTEM, user-friendly software for single-particle image processing. *Elife*. 7.

Hamilton, E.S., G.S. Jensen, G. Maksaev, A. Katims, A.M. Sherp, and E.S. Haswell. 2015a. Mechanosensitive channel MSL8 regulates osmotic forces during pollen hydration and germination. *Science*. 350:438-441.

Hamilton, E.S., A.M. Schlegel, and E.S. Haswell. 2015b. United in diversity: mechanosensitive ion channels in plants. *Annu Rev Plant Biol*. 66:113-137.

Haswell, E.S., R. Phillips, and D.C. Rees. 2011. Mechanosensitive channels: what can they do and how do they do it? *Structure*. 19:1356-1369.

Heymann, J.B., and D.M. Belnap. 2007. Bsoft: image processing and molecular modeling for electron microscopy. *J Struct Biol*. 157:3-18.

Higgins, A.J., A.J. Flynn, A. Marconnet, L.J. Musgrove, V.L.G. Postis, J.D. Lippiat, C.-w. Chung, T. Ceska, M. Zoonens, F. Sobott, and S.P. Muench. 2021. Cycloalkane-modified amphiphilic polymers provide direct extraction of membrane proteins for CryoEM analysis. *Communications Biology*. 4:1337.

Huang, C.-h., and S. Li. 1999. Calorimetric and molecular mechanics studies of the thermotropic phase behavior of membrane phospholipids. *Biochimica et Biophysica Acta (BBA) - Reviews on Biomembranes*. 1422:273-307.

Humphrey, W., A. Dalke, and K. Schulten. 1996. VMD: visual molecular dynamics. *J.Mol.Graph.* 14:33-38.

Iscla, I., R. Wray, and P. Blount. 2008. On the structure of the N-terminal domain of the MscL channel: helical bundle or membrane interface. *Biophys J*. 95:2283-2291.

Iudin, A., P.K. Korir, S. Somasundharam, S. Weyand, C. Cattavitello, N. Fonseca, O. Salih, Gerard J. Kleywegt, and A. Patwardhan. 2022. EMPIAR: the Electron Microscopy Public Image Archive. *Nucleic Acids Research*. 51:D1503-D1511.

Johansen, N.T., F.G. Tidemand, M.C. Pedersen, and L. Arleth. 2023. Travel light: Essential packing for membrane proteins with an active lifestyle. *Biochimie*. 205:3-26.

Jojoa-Cruz, S., K. Saotome, C.C.A. Tsui, W.H. Lee, M.S.P. Sansom, S.E. Murthy, A. Patapoutian, and A.B. Ward. 2022. Structural insights into the Venus flytrap mechanosensitive ion channel Flycatcher1. *Nat Commun*. 13:850.

Kamaraju, K., V. Belyy, I. Rowe, A. Anishkin, and S. Sukharev. 2011. The pathway and spatial scale for MscS inactivation. *Journal of General Physiology*. 138:49-57.

Knowles, T.J., R. Finka, C. Smith, Y.-P. Lin, T. Dafforn, and M. Overduin. 2009. Membrane Proteins Solubilized Intact in Lipid Containing Nanoparticles Bounded by Styrene Maleic Acid Copolymer. *Journal of the American Chemical Society*. 131:7484-7485.

Kopf, A.H., J.M. Dörr, M.C. Koorengevel, F. Antoniciello, H. Jahn, and J.A. Killian. 2020. Factors influencing the solubilization of membrane proteins from Escherichia coli membranes by styrene–maleic acid copolymers. *Biochimica et Biophysica Acta (BBA) - Biomembranes*. 1862:183125.

Levina, N., S. Totemeyer, N.R. Stokes, P. Louis, M.A. Jones, and I.R. Booth. 1999. Protection of Escherichia coli cells against extreme turgor by activation of MscS and MscL mechanosensitive channels: identification of genes required for MscS activity. *EMBO J.* 18:1730-1737.

Li, Y., P.C. Moe, S. Chandrasekaran, I.R. Booth, and P. Blount. 2002. Ionic regulation of MscK, a mechanosensitive channel from Escherichia coli. *EMBO J.* 21:5323-5330.

Liebschner, D., P.V. Afonine, M.L. Baker, G. Bunkóczi, V.B. Chen, T.I. Croll, B. Hintze, L.W. Hung, S. Jain, A.J. McCoy, N.W. Moriarty, R.D. Oeffner, B.K. Poon, M.G. Prisant, R.J. Read, J.S. Richardson, D.C. Richardson, M.D. Sammito, O.V. Sobolev, D.H. Stockwell, T.C. Terwilliger, A.G. Urzhumtsev, L.L. Videau, C.J. Williams, and P.D. Adams. 2019. Macromolecular structure determination using X-rays, neutrons and electrons: recent developments in Phenix. *Acta Crystallogr D Struct Biol*. 75:861-877.

Martinac, B., M. Buechner, A.H. Delcour, J. Adler, and C. Kung. 1987. Pressure-sensitive ion channel in Escherichia coli. *Proc.Natl.Acad.Sci.U.S.A*. 84:2297-2301.

Mastronarde, D.N. 2005. Automated electron microscope tomography using robust prediction of specimen movements. *J Struct Biol*. 152:36-51.

Moe, P., and P. Blount. 2005. Assessment of Potential Stimuli for Mechano-Dependent Gating of MscL: Effects of Pressure, Tension, and Lipid Headgroups. *Biochemistry*. 44:12239-12244.

Nomura, T., C.G. Cranfield, E. Deplazes, D.M. Owen, A. Macmillan, A.R. Battle, M. Constantine, M. Sokabe, and B. Martinac. 2012. Differential effects of lipids and lyso-lipids on the mechanosensitivity of the mechanosensitive channels MscL and MscS. *Proceedings of the National Academy of Sciences*. 109:8770-8775.

Park, Y.C., B. Reddy, N. Bavi, E. Perozo, and J.D. Faraldo-Gómez. 2023. State-specific morphological deformations of the lipid bilayer explain mechanosensitive gating of MscS ion channels. *eLife*. 12:e81445.

Pettersen, E.F., T.D. Goddard, C.C. Huang, E.C. Meng, G.S. Couch, T.I. Croll, J.H. Morris, and T.E. Ferrin. 2021. UCSF ChimeraX: Structure visualization for researchers, educators, and developers. *Protein Sci*. 30:70-82.

Pivetti, C.D., M.R. Yen, S. Miller, W. Busch, Y.H. Tseng, I.R. Booth, and M.H. Saier, Jr. 2003. Two families of mechanosensitive channel proteins. *Microbiol.Mol.Biol.Rev.* 67:66-85, table.

Pliotas, C., A.C. Dahl, T. Rasmussen, K.R. Mahendran, T.K. Smith, P. Marius, J. Gault, T. Banda, A. Rasmussen, S. Miller, C.V. Robinson, H. Bayley, M.S. Sansom, I.R. Booth, and J.H. Naismith. 2015. The role of lipids in mechanosensation. *Nat Struct Mol Biol*. 22:991-998.

Punjani, A., J.L. Rubinstein, D.J. Fleet, and M.A. Brubaker. 2017. cryoSPARC: algorithms for rapid unsupervised cryo-EM structure determination. *Nature Methods*. 14:290-296.

Punjani, A., H. Zhang, and D.J. Fleet. 2020. Non-uniform refinement: adaptive regularization improves single-particle cryo-EM reconstruction. *Nature Methods*. 17:1214-1221.

Qiu, W., Z. Fu, G.G. Xu, R.A. Grassucci, Y. Zhang, J. Frank, W.A. Hendrickson, and Y. Guo. 2018. Structure and activity of lipid bilayer within a membrane-protein transporter. *Proceedings of the National Academy of Sciences*. 115:12985-12990.

Rasmussen, T., V.J. Flegler, A. Rasmussen, and B. Böttcher. 2019. Structure of the Mechanosensitive Channel MscS Embedded in the Membrane Bilayer. *Journal of Molecular Biology*. 431:3081-3090.

Rath, A., M. Glibowicka, V.G. Nadeau, G. Chen, and C.M. Deber. 2009. Detergent binding explains anomalous SDS-PAGE migration of membrane proteins. *Proceedings of the National Academy of Sciences*. 106:1760-1765.

Ratkeviciute, G., B.F. Cooper, and T.J. Knowles. 2021. Methods for the solubilisation of membrane proteins: the micelle-aneous world of membrane protein solubilisation. *Biochemical Society Transactions*. 49:1763-1777.

Reddy, B., N. Bavi, A. Lu, Y. Park, and E. Perozo. 2019. Molecular basis of force-from-lipids gating in the mechanosensitive channel MscS. *Elife*. 8.

Ridone, P., Y. Nakayama, B. Martinac, and A.R. Battle. 2015. Patch clamp characterization of the effect of cardiolipin on MscS of E. coli. *Eur Biophys J*. 44:567-576.

Rohou, A., and N. Grigorieff. 2015. CTFFIND4: Fast and accurate defocus estimation from electron micrographs. *J Struct Biol*. 192:216-221.

Sotomayor, M., and K. Schulten. 2004. Molecular dynamics study of gating in the mechanosensitive channel of small conductance MscS. *Biophys.J.* 87:3050-3065.

Sukharev, S. 2002. Purification of the Small Mechanosensitive Channel of Escherichia coli (MscS): the Subunit Structure, Conduction, and Gating Characteristics in Liposomes. *Biophysical Journal*. 83:290-298.

Sukharev, S.I., B. Martinac, V.Y. Arshavsky, and C. Kung. 1993. Two types of mechanosensitive channels in the Escherichia coli cell envelope: solubilization and functional reconstitution. *Biophys J*. 65:177-183.

Sukharev, S.I., W.J. Sigurdson, C. Kung, and F. Sachs. 1999. Energetic and spatial parameters for gating of the bacterial large conductance mechanosensitive channel, MscL. *J.Gen.Physiol*. 113:525-540.

Sun, C., S. Benlekbir, P. Venkatakrishnan, Y. Wang, S. Hong, J. Hosler, E. Tajkhorshid, J.L. Rubinstein, and R.B. Gennis. 2018. Structure of the alternative complex III in a supercomplex with cytochrome oxidase. *Nature*. 557:123-126.

Veley, K.M., S. Marshburn, C.E. Clure, and E.S. Haswell. 2012. Mechanosensitive channels protect plastids from hypoosmotic stress during normal plant growth. *Curr Biol*. 22:408-413.

Wang, W., S.S. Black, M.D. Edwards, S. Miller, E.L. Morrison, W. Bartlett, C. Dong, J.H. Naismith, and I.R. Booth. 2008. The structure of an open form of an E. coli mechanosensitive channel at 3.45 A resolution. *Science*. 321:1179-1183.

Williams, C.J., J.J. Headd, N.W. Moriarty, M.G. Prisant, L.L. Videau, L.N. Deis, V. Verma, D.A. Keedy, B.J. Hintze, V.B. Chen, S. Jain, S.M. Lewis, W.B. Arendall III, J. Snoeyink, P.D. Adams, S.C. Lovell, J.S. Richardson, and D.C. Richardson. 2018. MolProbity: More and better reference data for improved all-atom structure validation. *Protein Science*. 27:293-315.

Wilson, M.E., G.S. Jensen, and E.S. Haswell. 2011. Two mechanosensitive channel homologs influence division ring placement in Arabidopsis chloroplasts. *Plant Cell*. 23:2939-2949.

Zhang, Y., C. Daday, R.-X. Gu, C.D. Cox, B. Martinac, B.L. de Groot, and T. Walz. 2021. Visualization of the mechanosensitive ion channel MscS under membrane tension. *Nature*. 590:509-514.

Zheng, S.Q., E. Palovcak, J.-P. Armache, K.A. Verba, Y. Cheng, and D.A. Agard. 2017. MotionCor2: anisotropic correction of beam-induced motion for improved cryo-electron microscopy. *Nature Methods*. 14:331-332.

Figures

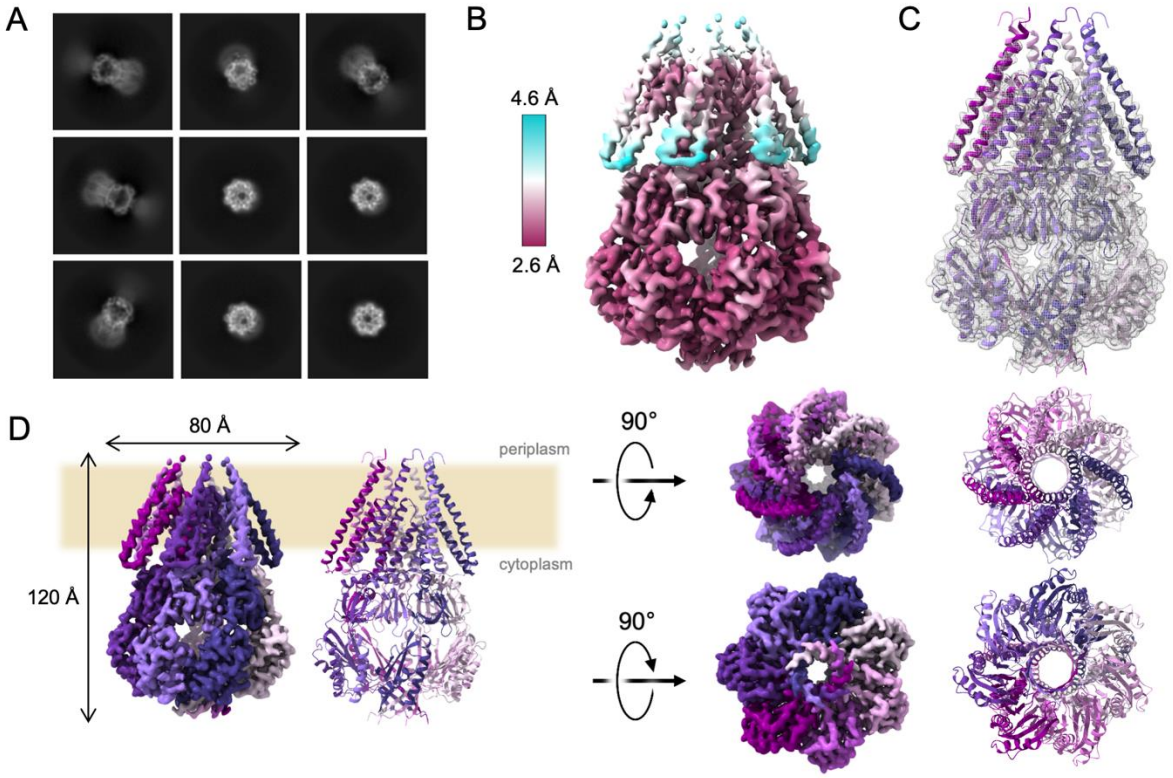

Figure 1: *E. coli* MscS cryo-EM structure in Glyco-DIBMA. (A) Selected 2D class averages of the particles used for the final reconstruction with a box size of 360 px (~300 Å). (B) Cryo-EM map filtered and colored by local resolution. (C) Fitted model in ribbon representation inside map shown in gray mesh. (D) Map and model colored by the seven chains shown as side view (left), top, and bottom view (right).

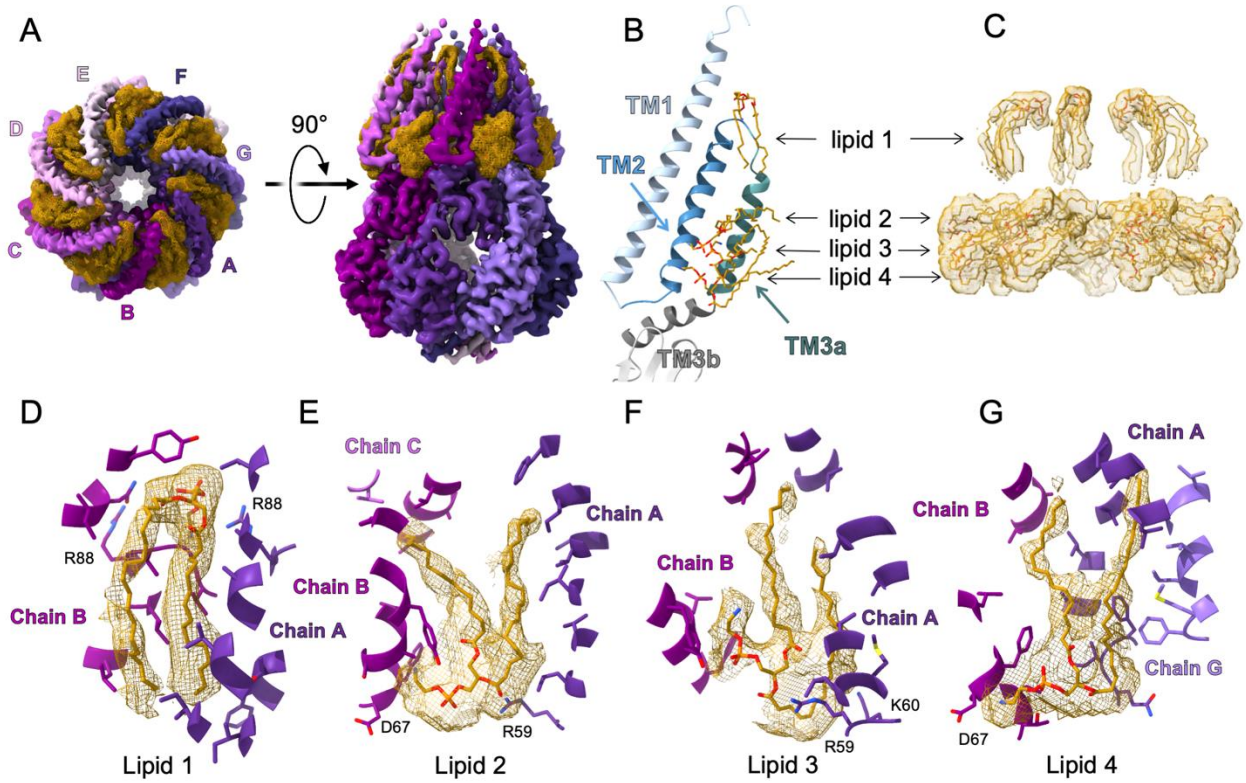

Figure 2: Resolved bound lipids in the TM region of *E. coli* MscS. (A) Map colored by chain in top (left) and side view (right) with lipid densities shown in yellow mesh. (B) Protein monomer colored by domain with the locations of modelled lipids. (C) Side view of lipid densities shown in mesh with modelled lipids in stick representation. Zoomed in view of lipid 1 (D), lipid 2 (E), lipid 3 (F) and lipid 4 (G) in mesh density shown with all residues within 5 Å within the modelled protein A full list of nearby residues is given in Supplemental Table 3.

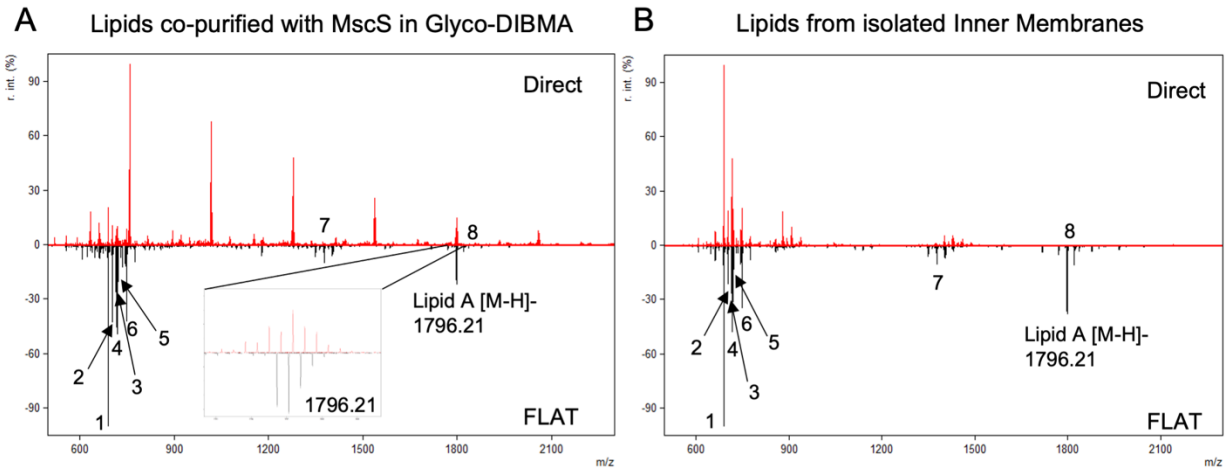

C

Number	Matched Mass	Name	Formula	Relative Intensity
1	688.49	PE 32:1	C37H72NO8P	100:100
2	702.51	PE 33:1	C38H74NO8P	42:21
3	714.51	PE 34:2	C39H74NO8P	26:26
4	716.52	PE 34:1	C39H76NO8P	46:48
5	719.49	PG 32:1	C38H73O10P	50:31
6	747.52	PG 34:1	C40H77O10P	43:34
7	1375.97	CL 66:2	C75H142O17P2	10:10
8	1796.21	Lipid A	C94H178N2O25P2	19:36

Figure 3: Lipid Mass Spectrometry. (A) Lipids co-purified with MscS using Glyco-DIBMA. (B) Lipids from isolated *E. coli* inner membranes. (C) Table comparing the relative amount of lipids between the two samples in A and B.

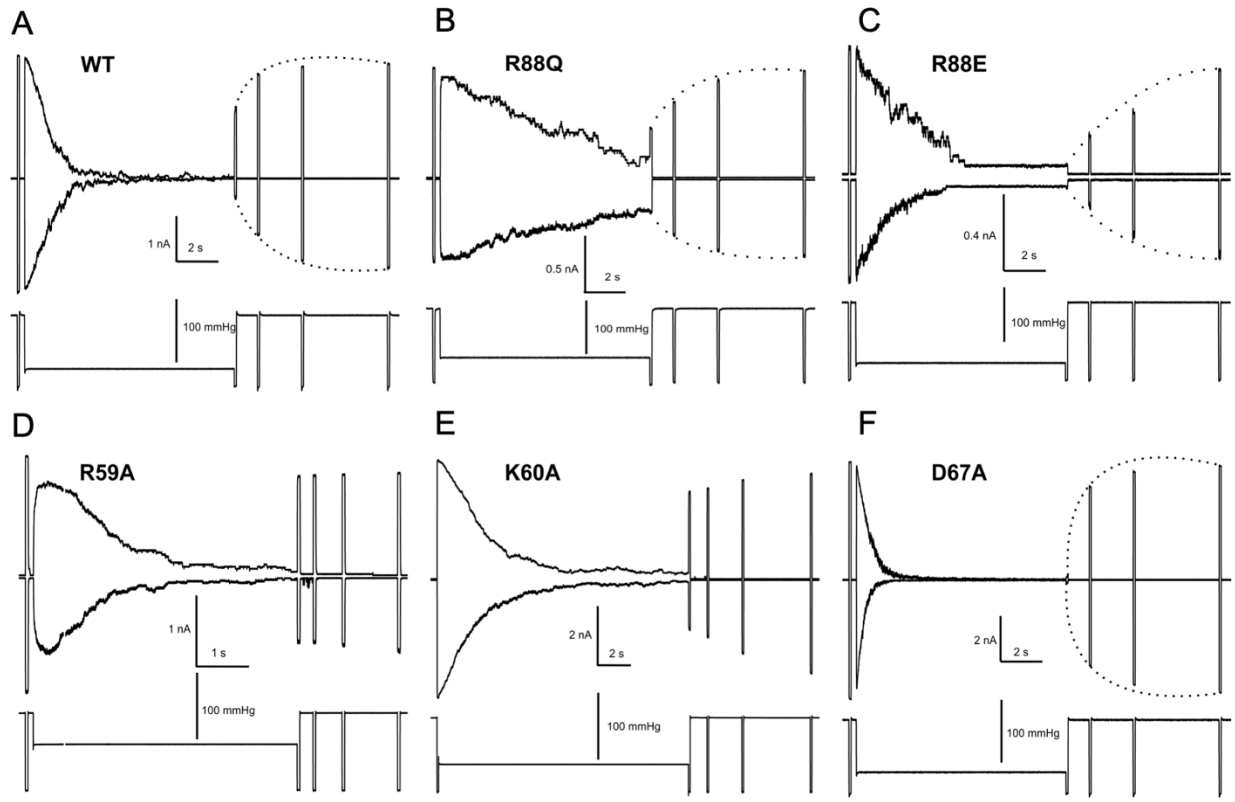

Figure 4: Patch-clamp traces recorded on giant *E. coli* spheroplasts with inactivation-recovery pressure protocols. The first short test pulse of saturating amplitude opens the entire population of channels, then the extended step of intermediate tension drives them toward inactivation. The following train of saturating test pulses monitors the fraction of remaining active channels, which is used to determine the kinetics of recovery. R88Q (B) behaves like WT (A), whereas R88E (C) exhibits significantly slowed recovery from inactivation (see Supplemental Table 4). The R59A mutant (D) is largely resistant to inactivation, whereas D67A (F) inactivates completely and recovers very quickly. K60A (E) is an intermediate phenotype similar to R59A but to a lesser degree.

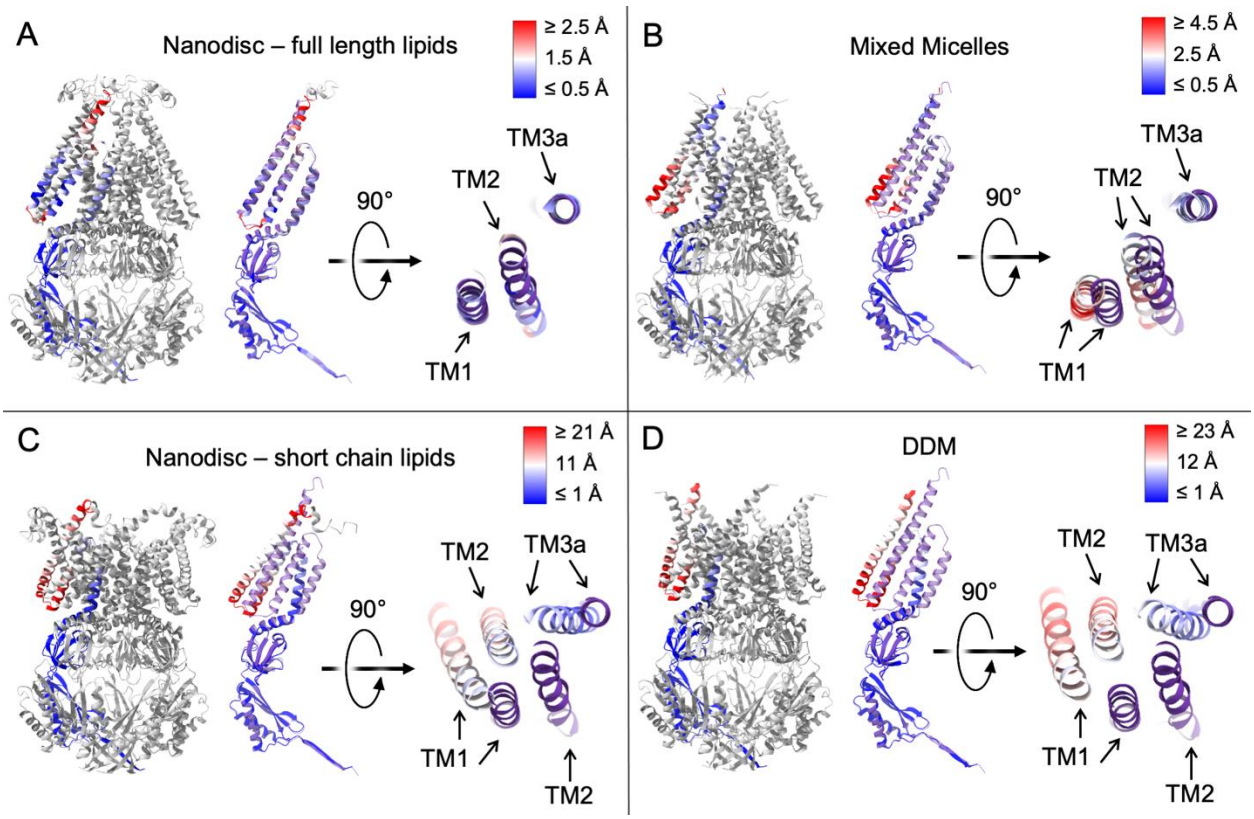

Figure 5: Structure Comparison. (A) MscS in nanodiscs with full length lipids (PDB 6PWN (Reddy et al., 2019)) shown in cartoon representation with chain A colored by RMSD to the Glyco-DIBMA extracted MscS structure (left). Comparison of one chain from each structure, with the Glyco-DIBMA extracted MscS in purple (middle). Top view comparing the TM helices (right). The average RMSD is 0.9 Å. (B) MscS in mixed micelles (PDB 7OO6 (Flegler et al., 2021)) shown in cartoon representation with chain A colored by RMSD to the Glyco-DIBMA extracted MscS structure (left). Comparison of one chain from each structure, with the Glyco-DIBMA extracted MscS in purple (middle). Top view comparing the TM helices (right). The average RMSD is 1.7 Å. (C) MscS in nanodiscs with short chain lipids (PDB 8DDJ (Park et al., 2023)) shown in cartoon representation with chain A colored by RMSD to the Glyco-DIBMA extracted MscS structure (left). Comparison of one chain from each structure, with the Glyco-DIBMA extracted MscS in purple (middle). Top view comparing the TM helices (right). The average RMSD is 8.6 Å. (B) MscS in DDM (PDB 7OO0 (Flegler et al., 2021)) shown in cartoon representation with chain A colored by RMSD to the Glyco-DIBMA extracted MscS structure (left). Comparison of one chain from each structure, with the Glyco-DIBMA extracted MscS in purple (middle). Top view comparing the TM helices (right). The average RMSD is 9.6 Å.

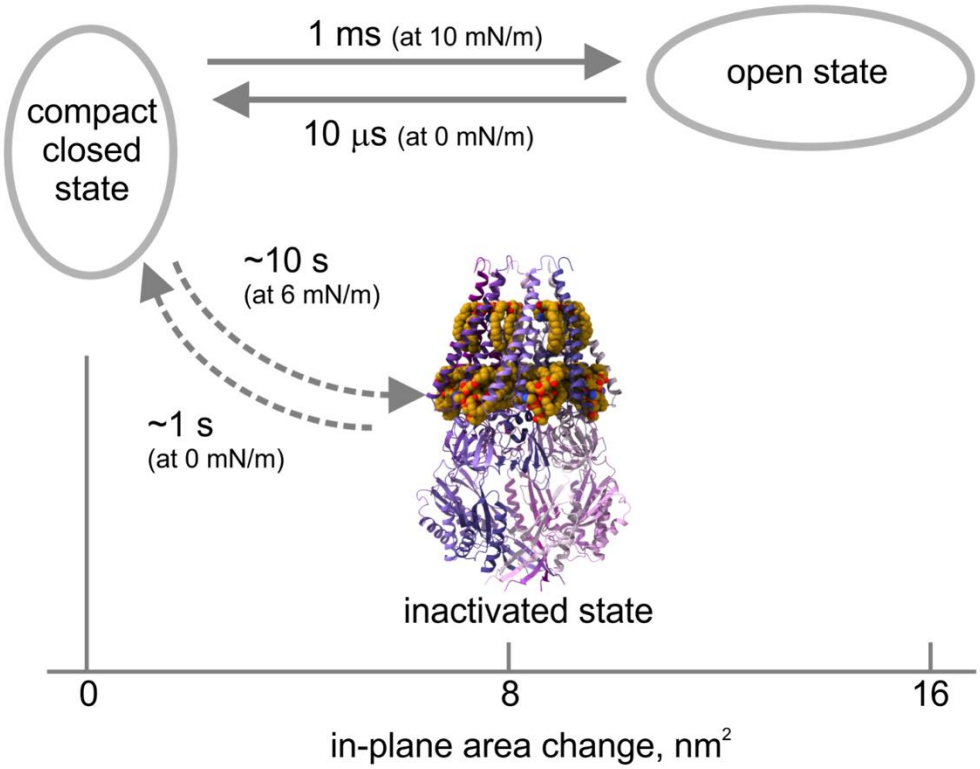

Figure 6. The experimentally determined kinetic scheme of MscS and the assignment of the newly solved structure. The opening-closing and inactivation-recovery pathways are characterized with different spatial scales and drastically different transition kinetics.

Supplementary Information

Polymer-extracted structure of the mechanosensitive channel MscS suggests a role of protein-lipid interactions in the gating cycle

Elissa Moller [1,2,3], Madolyn Britt [2,3], Fei Zhou [1], Hyojik Yang[4], Andriy Anshkin[3], Robert Ernst [4], Sergei Sukharev [2,3,5,#], Doreen Matthies [1,#]

[1] Unit on Structural Biology, Division of Basic and Translational Biophysics, *Eunice Kennedy Shriver* National Institute of Child Health and Human Development, National Institutes of Health, Bethesda, MD, USA.

[2] Biophysics Graduate Program, University of Maryland, College Park, MD, USA.

[3] Department of Biology, University of Maryland, College Park, MD, USA.

[4] Department of Microbial Pathogenesis, University of Maryland, Baltimore, MD, USA.

[5] Institute for Physical Science and Technology, University of Maryland, College Park, MD, USA.

Correspondence to Sergei Sukharev (sukharev@umd.edu) and Doreen Matthies (Doreen.Matthies@nih.gov)

Supplemental Figure 1: Membrane protein extraction methods for structural studies.

Supplemental Figure 2: Glyco-DIBMA biochemical characterization and negative staining EM.

Supplemental Figure 3: SMALP 200 biochemical characterization and negative staining EM.

Supplemental Figure 4: CyclAPol C_8-C_0-50 biochemical characterization and negative staining EM.

Supplemental Figure 5: Glyco-DIBMA #1 cryo-EM workflow.

Supplemental Figure 6: Glyco-DIBMA #2 cryo-EM workflow.

Supplemental Figure 7: SMALP 200 #1 cryo-EM workflow.

Supplemental Figure 8: SMALP 200 #2 cryo-EM workflow.

Supplemental Figure 9: CyclAPol C_8-C_0-50 cryo-EM workflow.

Supplemental Figure 10: Negative staining EM of Polymers.

Supplemental Figure 11: Comparison of 2D class averages and maps of the different polymers.

Supplemental Figure 12: Quality of the cryo-EM map and fitted model of MscS in Glyco-DIBMA.

Supplemental Figure 13: Liposome-like 2D class averages and models.

Supplemental Figure 14: Extra Densities of MscS in Glyco-DIBMA.

Supplemental Figure 15: Structure Comparison.

Supplemental Table 1: Cryo-EM data collection parameters and analysis.

Supplemental Table 2: Cryo-EM map and model analysis.

Supplemental Table 3: Residues within 5 Å of modelled lipids.

Supplemental Table 4: Summary of patch clamp data.

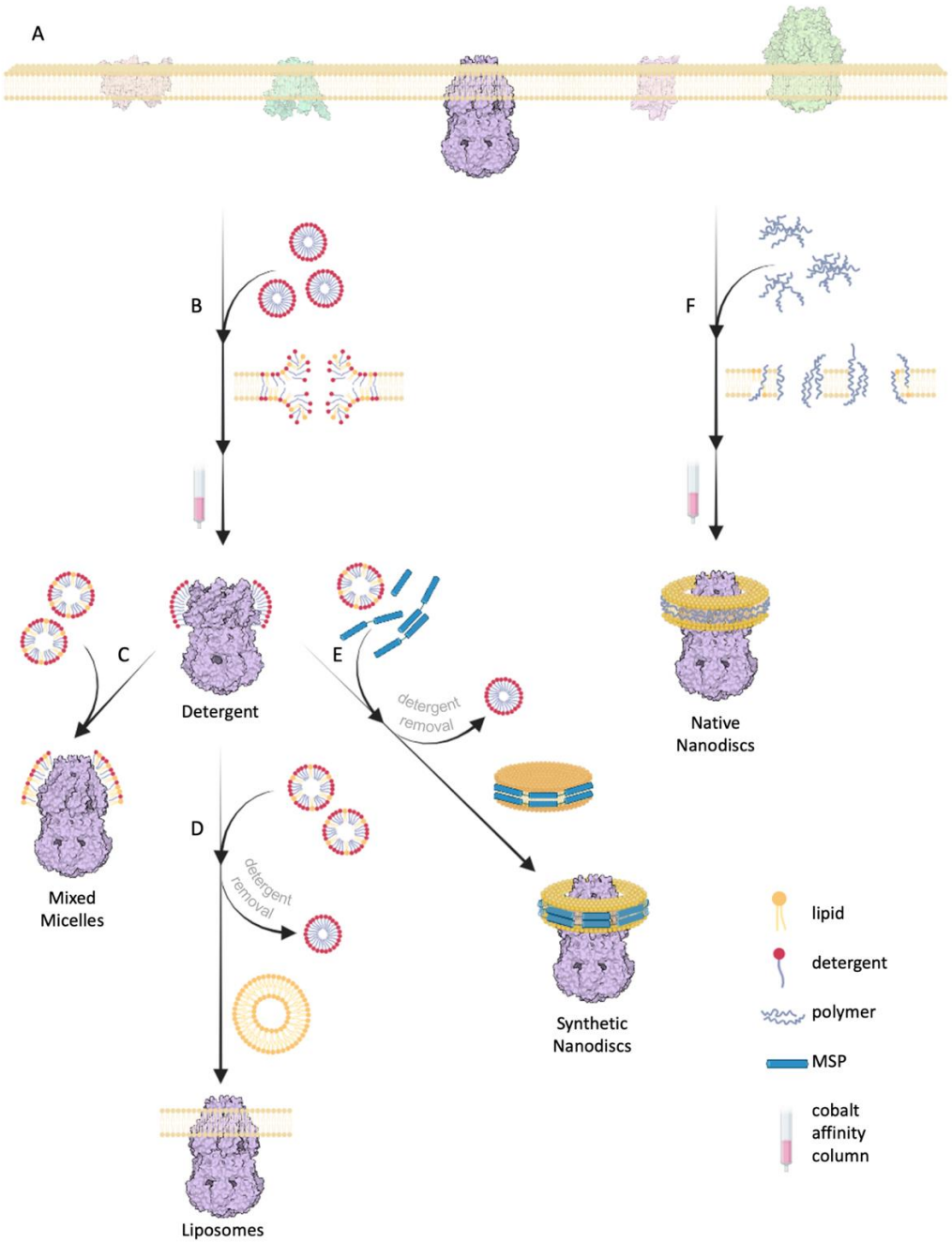

Supplemental Figure 1: Membrane protein extraction methods for structural studies. (A) Membrane proteins in the bilayer (left to right PDBs 1KPK, 1PW4, 2OAU, 1PV6, and 1IWG). (B) Detergent solubilization leading to a conductive conformation of MscS (PDB 2VV5), followed by affinity chromatography. (C) Direct membrane protein extraction using polymers, followed by affinity chromatography. (D) Addition of detergent solubilized lipids to form mixed micelles leading to a non-conductive conformation of MscS (PDB 2OAU). (E) Addition of detergent solubilized lipids followed by detergent removal for liposome reconstitution leading to a non-conductive conformation of MscS (PDB 2OAU). (F) Addition of detergent solubilized membrane scaffold protein (MSP) and lipids followed by detergent removal for synthetic nanodisc reconstitution leading to a non-conductive conformation of MscS (PDB 2OAU). Created with BioRender.com.

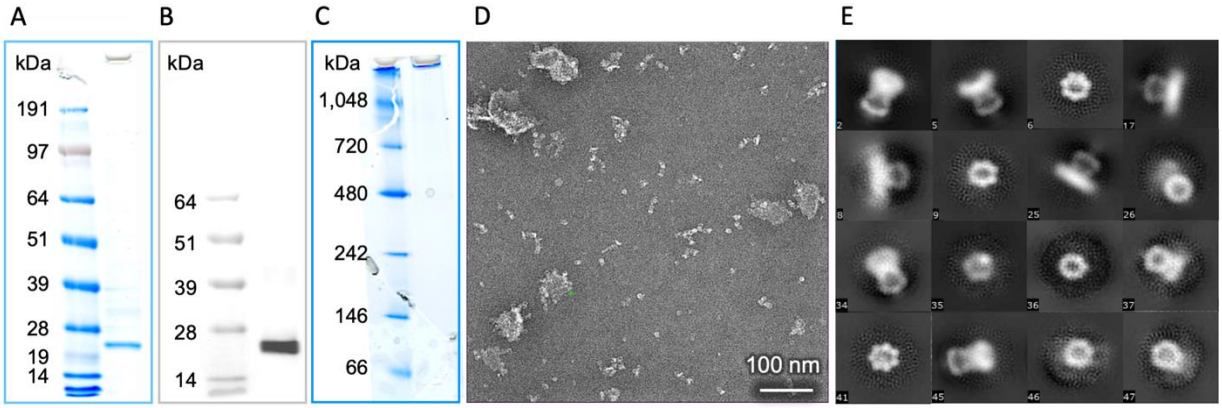

Supplemental Figure 2: MscS in Glyco-DIBMA biochemical characterization and negative staining EM. (A) SDS gel indicating the 31 kDa MscS monomer running between the 19 and 28 kDa marker bands. (B) Western Blot. (C) BN-PAGE gel not indicating a nice band at the expected MW of 217 kDa for the MscS heptamer but signal in the gel loading pocket. (D) Representative negative staining electron micrograph of MscS extracted with 0.5% Glyco-DIBMA indicating some isolated single particles as well as small vesicle- or membrane-patch like particles. (E) Selected 2D class averages with a box size of 168 px (~250 Å).

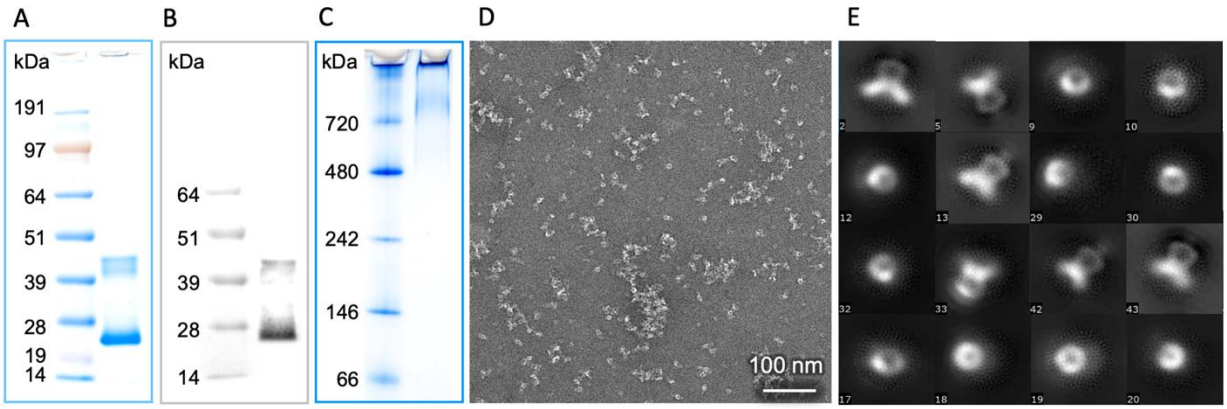

Supplemental Figure 3: MscS in SMALP 200 biochemical characterization and negative staining EM. (A) SDS gel indicating the 31 kDa MscS monomer running between the 19 and 28 kDa marker bands. (B) Western Blot (C) BN-PAGE gel not indicating a nice band at the expected MW of 217 kDa for the MscS heptamer but signal in the gel loading pocket. (D) Representative negative staining electron micrograph of MscS extracted with 1% SMALP 200 indicating some isolated single particles as well as aggregation. (E) Selected 2D class averages with a box size of 168 px (~250 Å).

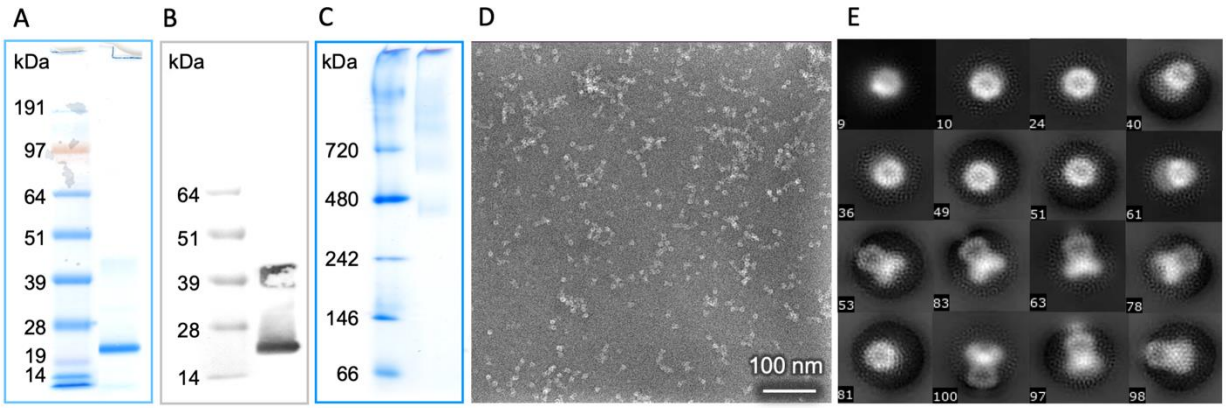

Supplemental Figure 4: MscS in CyclAPol C_8-C_0-50 biochemical characterization and negative staining EM. (A) SDS gel indicating the 31 kDa MscS monomer running between the 19 and 28 kDa marker bands. (B) Western Blot (C) BN-PAGE gel not indicating a nice band at the expected MW of 217 kDa for the MscS heptamer but signal in the gel loading pocket. (D) Representative negative staining electron micrograph of MscS extracted with 0.1% CyclAPol C_8-C_0-50 indicating some isolated single particles with some aggregation. (E) Selected 2D class averages with a box size of 168 px (~250 Å).

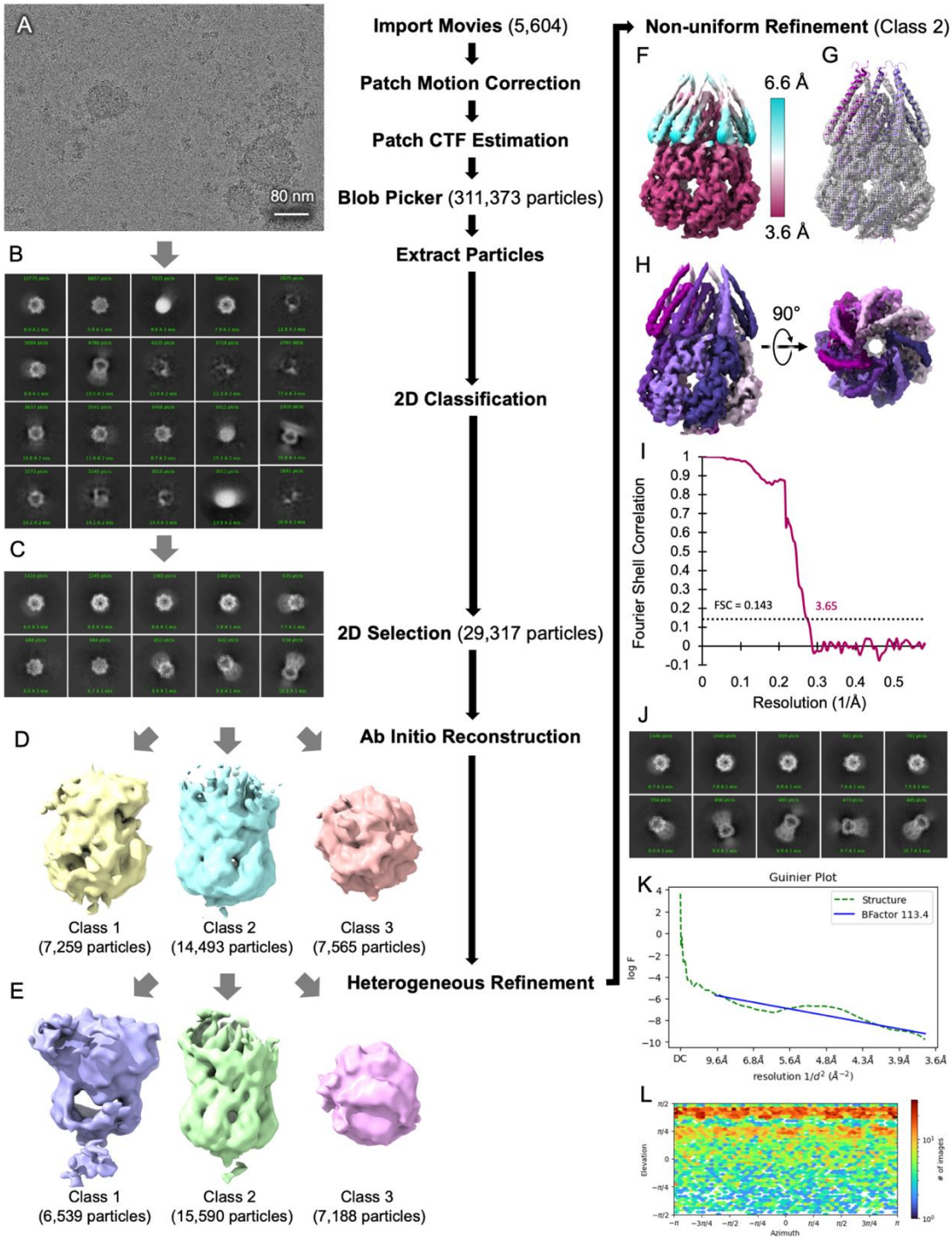

Supplemental Figure 5: Glyco-DIBMA #1 cryo-EM workflow. (A) Representative cryo-EM micrograph (B) Representative 2D class averages from the initial particle picking with a box size of 360 px (~300 Å). (C) Selected 2D class averages of particles used for *Ab Initio* Reconstruction, note the unique top view 2D class averages in the bottom left row. (D) *Ab Initio* reconstructions. (E) Heterogeneous Refinement. (F) Non-uniform refinement of Class 2 in E with C7 symmetry filtered and colored by local resolution. (G) Final MscS model rigid body fit into map shown in gray mesh. (H) Map colored by chain, side view (left) and top view (right). (I) FSC curve. (J) Representative 2D class averages of particles used for final reconstruction. (K) Guinier Plot. (L) Viewing Directions.

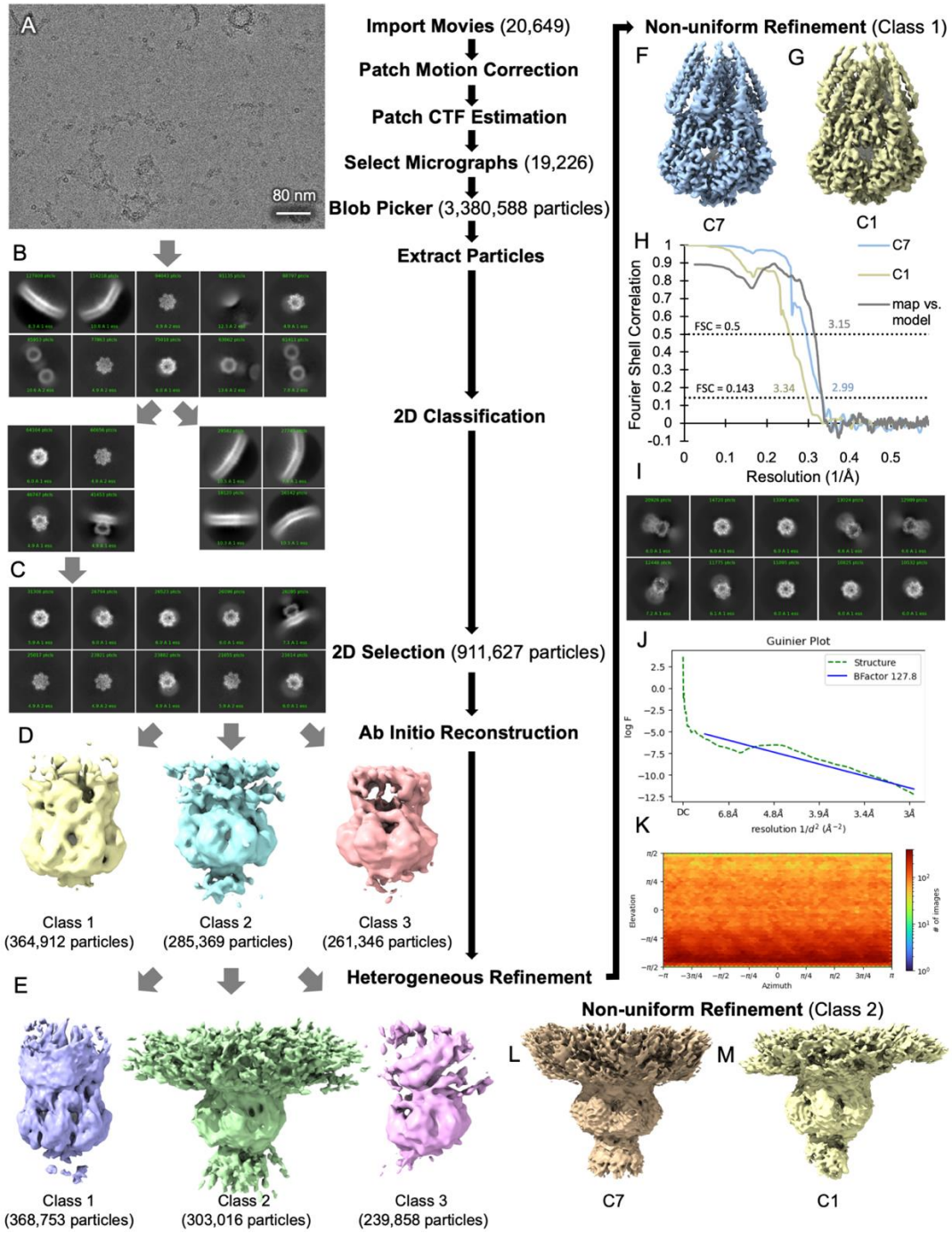

Supplemental Figure 6: Glyco-DIBMA #2 cryo-EM workflow. (A) Representative cryo-EM micrograph (B) Representative 2D class averages from the initial particle picking with a box size of 360 px (~300 Å), note the unique top view 2D class averages in the middle of the top row and second from the left in the bottom row. (C) Selected 2D class averages of particles used for *Ab Initio* Reconstruction. (D) *Ab Initio* Reconstructions (E) Heterogeneous Refinement (F) Non-uniform refinement of Class 1 in E with C7 symmetry. (G) Non-uniform refinement of Class 1 in E with C1 symmetry. (H) FSC curve for C7 (blue), C1 (yellow), and map vs. model (gray). (I) Representative 2D class averages of particles used for final reconstruction. (J) Guinier Plot. (K) Viewing Directions. (L) Non-uniform refinement for Class 2 in E with C7 symmetry. (M) Non-uniform refinement for Class 2 in E with C1 symmetry.

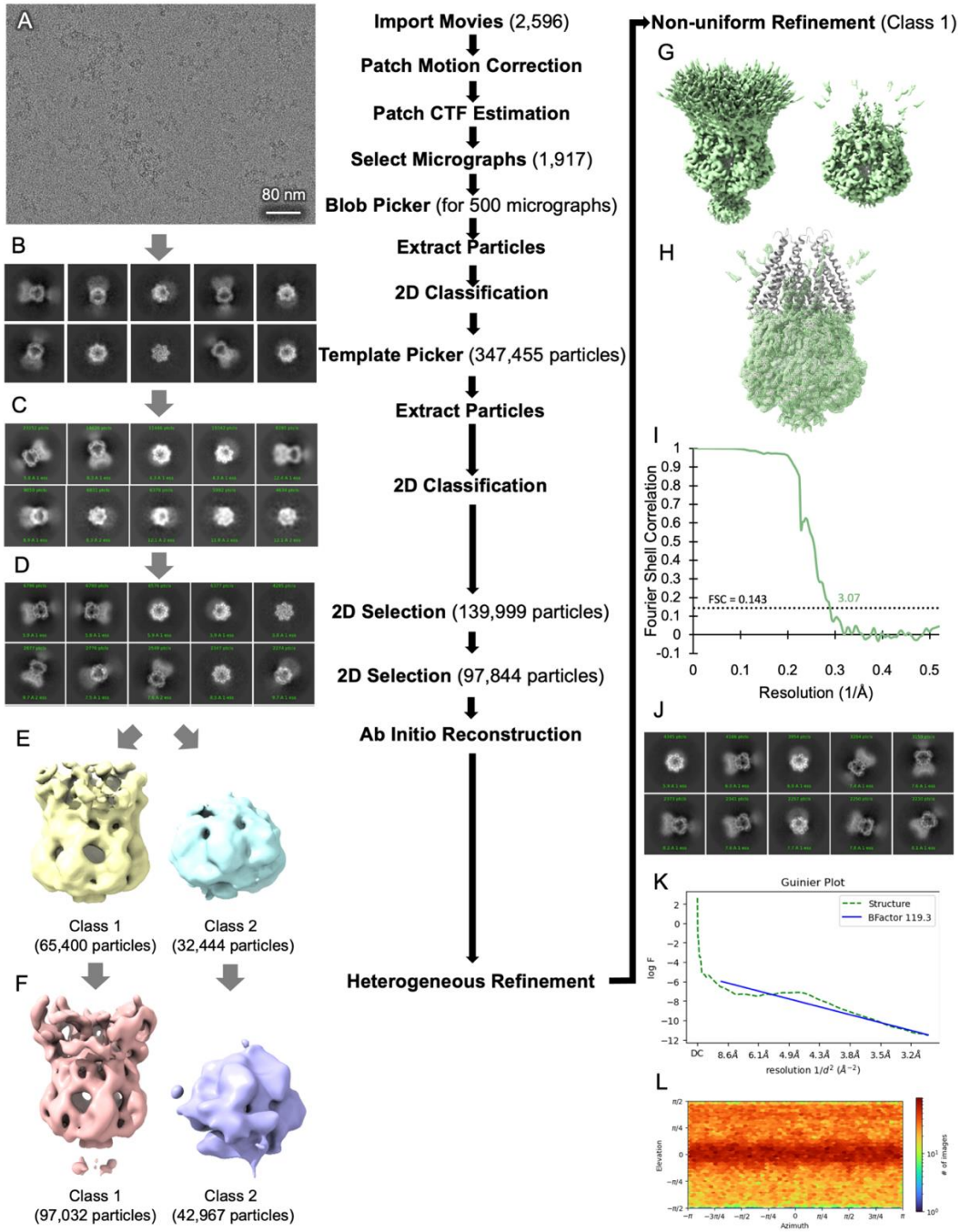

Supplemental Figure 7: SMALP 200 #1 cryo-EM workflow. (A) Representative cryo-EM micrograph (B) 2D class averages used for template picking, generated from using blob picker on 500 micrographs with a box size of 640 px (~270 Å) Fourier cropped to box size of 320 px, note the unique top view 2D class average in the middle of the bottom row. (C) Representative 2D class averages from the initial particle picking. (D) Selected 2D class averages of particles later used for Heterogeneous Refinement in F. (E) *Ab Initio* Reconstructions using a subset of 97,844 particles. (F) Heterogeneous Refinement with all the particles in C (139,999). (G) Non-uniform refinement of Class 1 in F with C7 symmetry at different thresholds. (H) Final MscS model rigid body fit into map shown in mesh. (I) FSC curve. (J) Representative 2D class averages of particles used for final reconstruction. (K) Guinier Plot. (L) Viewing Directions.

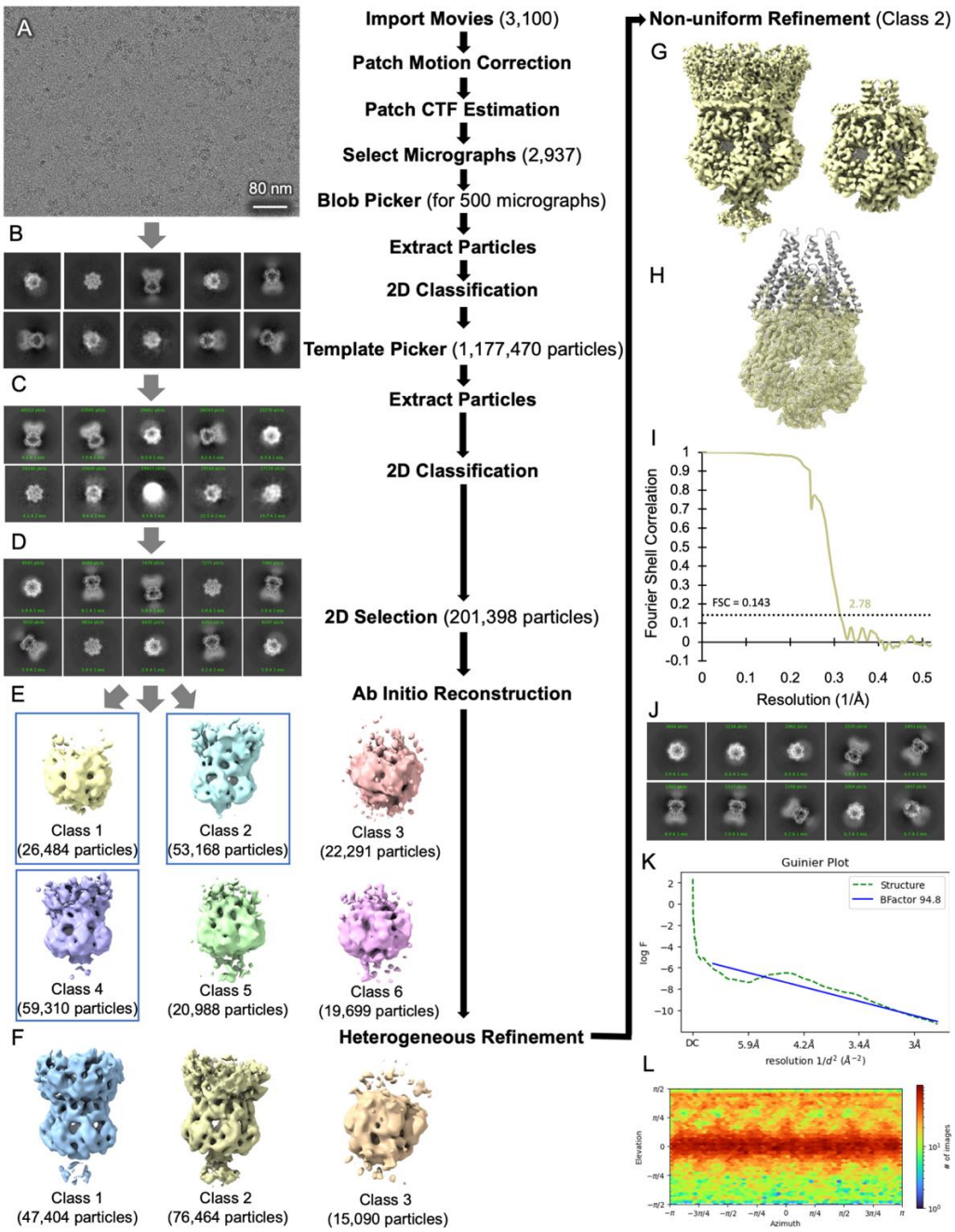

Supplemental Figure 8: SMALP 200 #2 cryo-EM workflow. (A) Representative cryo-EM micrograph (B) 2D class averages used for template picking, generated from using blob picker on 500 micrographs with a box size of 640 px (~270 Å) Fourier cropped to box size of 320 px, note the unique top view 2D class average second from the left in the top row. (C) Representative 2D class averages from the initial particle picking. (D) Selected 2D class averages of particles used for *Ab Initio* Reconstruction. (E) *Ab Initio* Reconstructions, particles and maps in blue boxes were used for Heterogeneous Refinement in F. (F) Heterogeneous Refinement of selected particles and maps from Class 1, 2, and 4 in E. (G) Non-uniform refinement of Class 1 in F with C7 symmetry at different thresholds. (H) Final MscS model rigid body fit into map shown in mesh. (I) FSC curve. (J) Representative 2D class averages of particles used for final reconstruction. (K) Guinier Plot. (L) Viewing Directions.

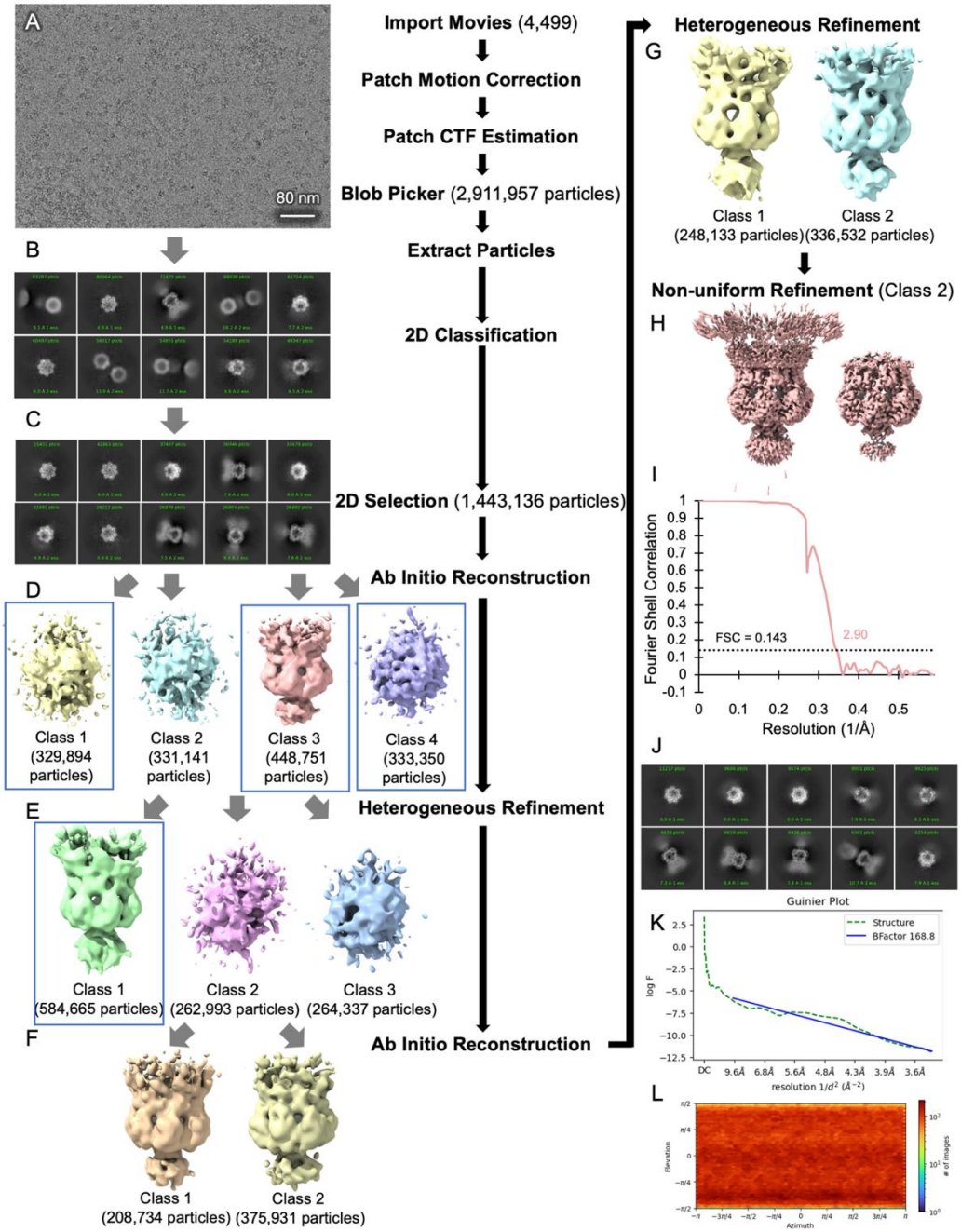

Supplemental Figure 9: CyclAPol C_8-C_0-50 cryo-EM workflow. (A) Representative cryo-EM micrograph (B) Representative 2D class averages from the initial particle picking with a box size of 360 px (~300 Å), note the unique top view 2D class averages second from the left in the top row and left in the bottom row. (C) Selected 2D class averages used for *Ab Initio* Reconstruction. (D) *Ab Initio* Reconstructions, particles and maps in blue boxes were used for Heterogeneous Refinement in E. (E) Heterogeneous Refinement of selected particles and maps from Class 1, 3, and 5 in D, particles from the map in the blue box were subjected to another round of *Ab Initio* Reconstruction in F. (F) Second round of *Ab Initio* Reconstruction with particles from Class 1 in F. (G) Heterogeneous Refinement with particles and maps from F. (H) Non-uniform refinement of Class 2 in G with C7 symmetry at different thresholds. (I) FSC curve. (J) Representative 2D class averages of particles used for final reconstruction. (K) Guinier Plot. (L) Viewing Directions.

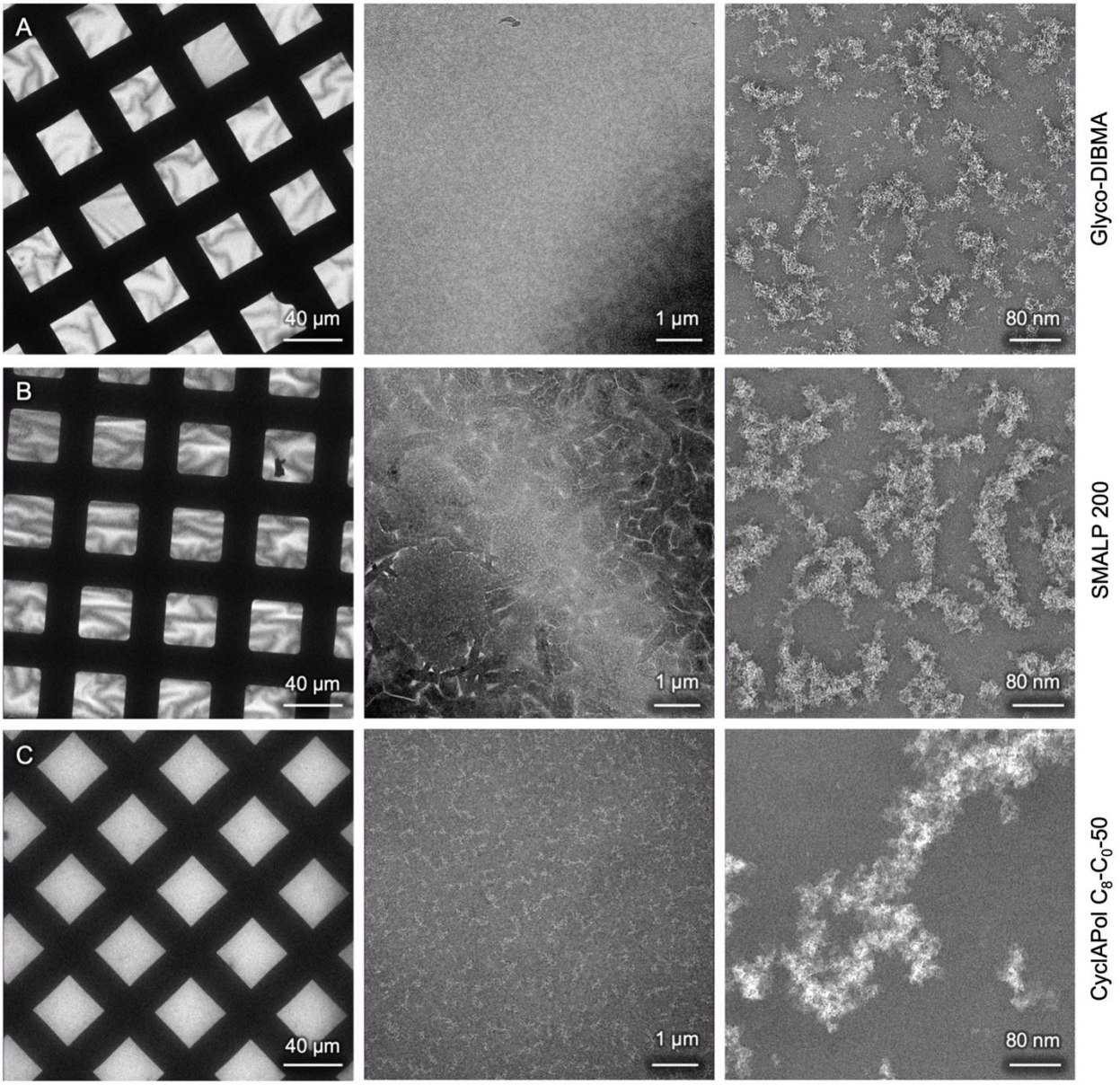

Supplemental Figure 10: Negative Staining EM of Polymers. (A) 0.5% Glyco-DIBMA in 20 mM HEPES pH 7.4 Membrane Buffer 1 at low magnification (left) medium magnification (middle) and high magnification (right). (B) 1% SMALP 200 in 20 mM Tris/HCl pH 8.0 Purification Buffer at low magnification (left) medium magnification (middle) and high magnification (right). (C) 0.1% CyclAPol C_8-C_0-50 in 20 mM Tris/HCl pH 8.0 Purification Buffer at low magnification (left) medium magnification (middle) and high magnification (right).

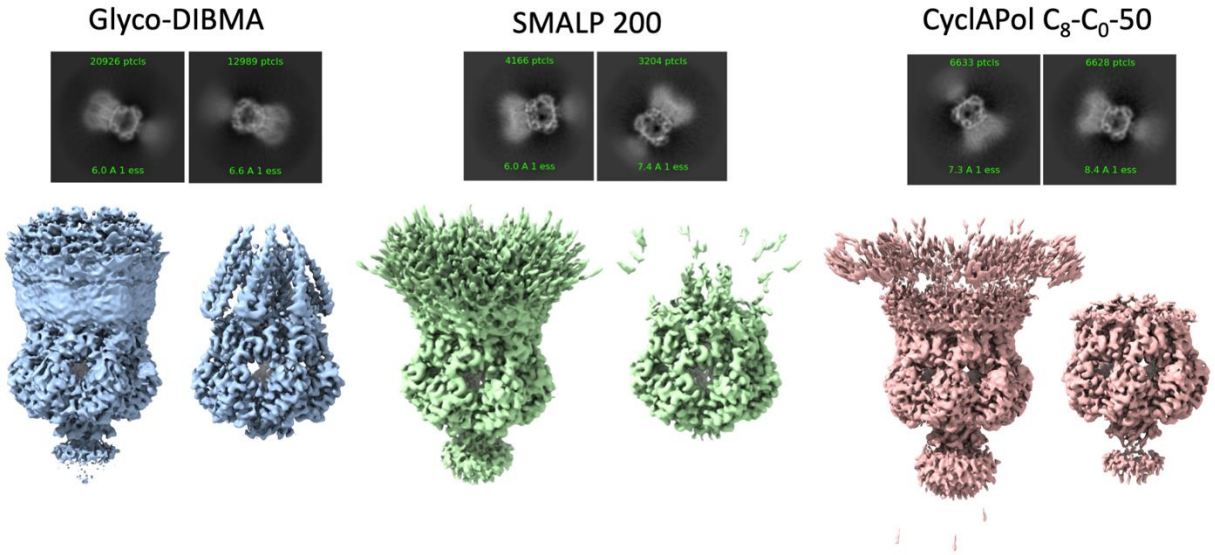

Supplemental Figure 11: Comparison of 2D class averages and maps of the different polymers. 2D class averages and 3D reconstruction at varying thresholds for Glyco-DIBMA (left), SMALP 200 (middle), and CyclAPol C_8-C_0-50 (right) extracted MscS.

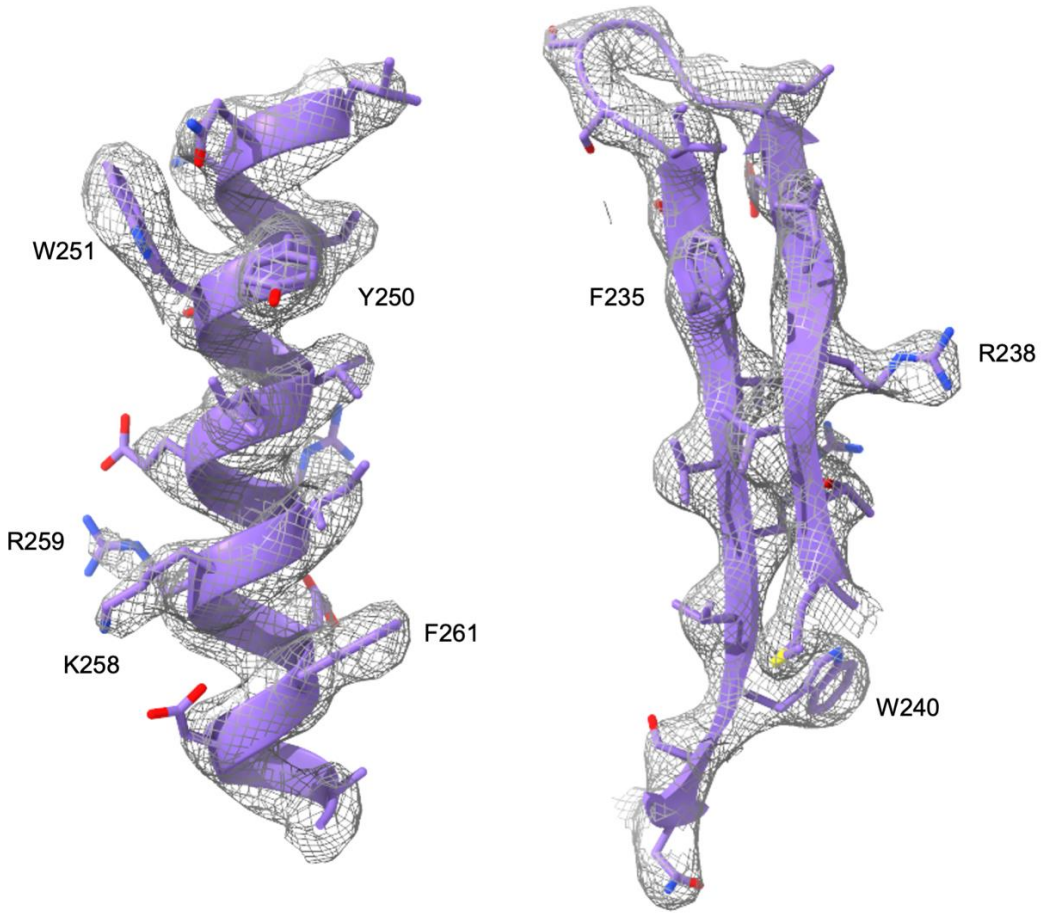

Supplemental Figure 12: Quality of the cryo-EM map and fitted model of MscS in Glyco-DIBMA. Representative densities of an α-helix (left) and a β-sheet (right) with fitted model in purple in ribbon representation and side chains in sticks.

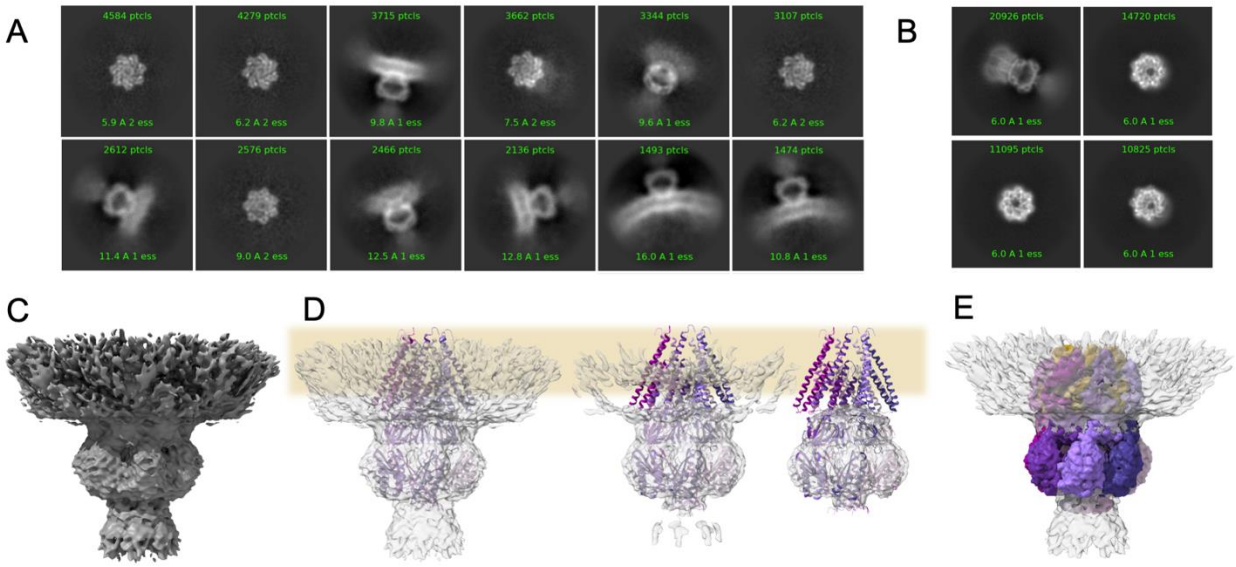

Supplemental Figure 13: Liposome-like 2D class averages and models. (A) Selected 2D class averages from Class 2 (Supplemental Figure 6D,E) containing the side views with a visible bilayer extending away from the protein and the unique tight and sharply star shaped top views without an opening for the pore. (B) Representative typical 2D class averages from Class 1 for comparison (Supplemental Figure 6D,E) that went into the final 3D reconstruction for Glyco-DIBMA extracted MscS. (C) Class 2 after non-uniform refinement (Supplemental Figure 6L). (D) Map from C with Glyco-DIBMA extracted MscS rigid body fit into the density, shown at varying thresholds. (E) Map from C colored by nearby residues based on the rigid body fit model.

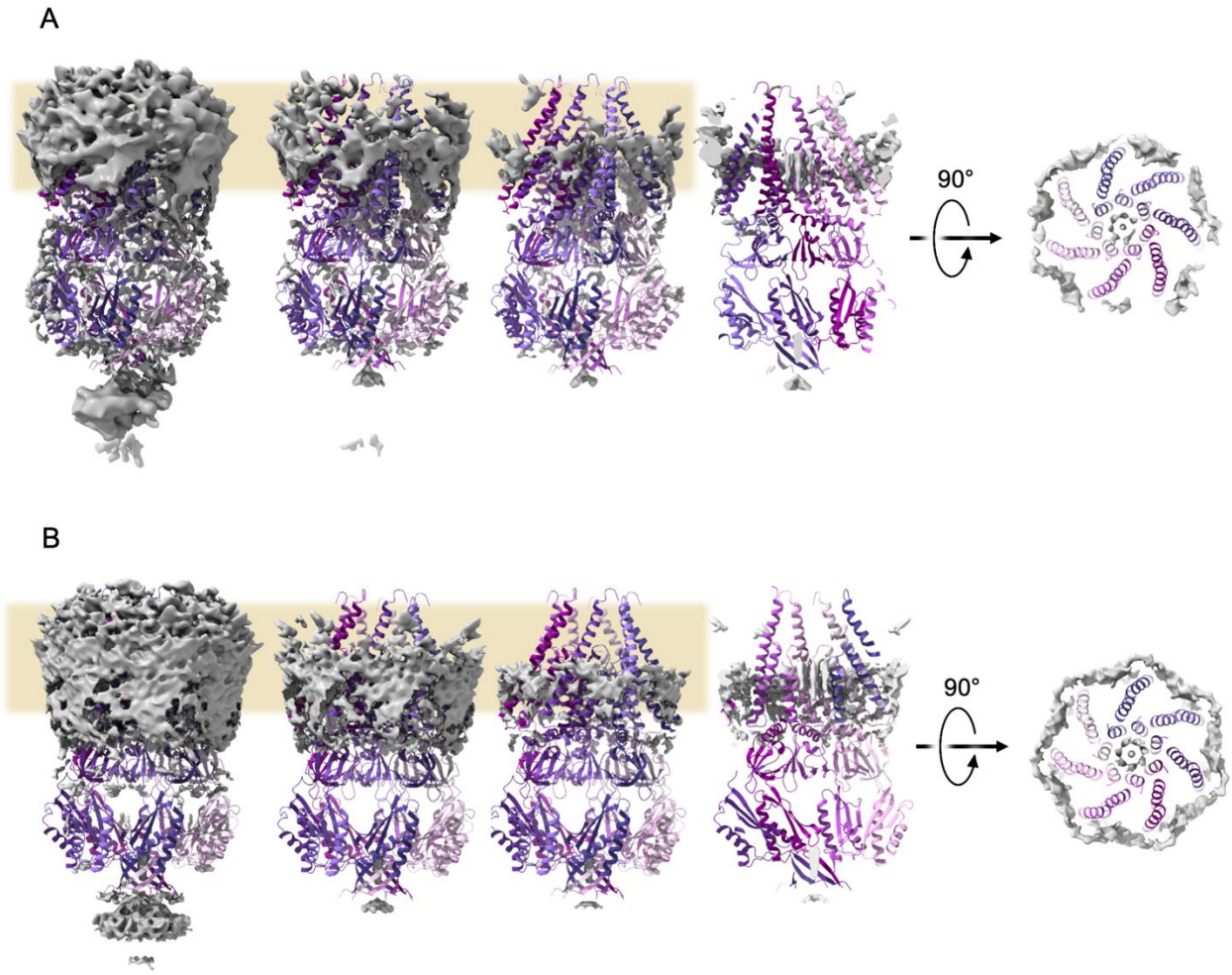

Supplemental Figure 14: Extra Densities of MscS in Glyco-DIBMA. (A) Additional densities not modelled as lipids in C1 symmetry at varying thresholds. (B) Additional densities not modelled as lipids in C7 symmetry at varying thresholds.

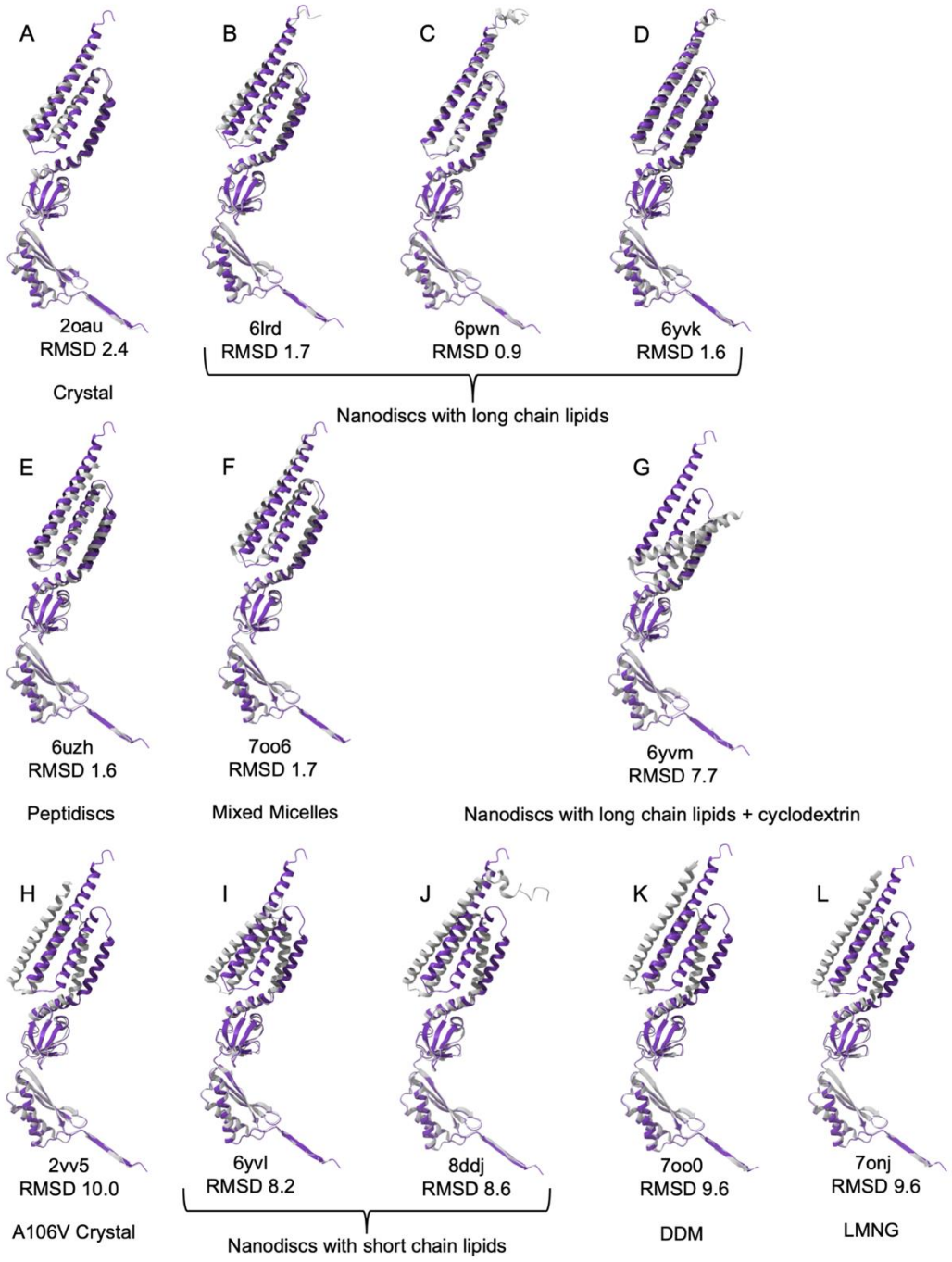

Supplemental Figure 16: Structure Comparison. (A) A single subunit of the original crystal structure (Bass et al., 2002) which has the characteristic non-conductive architecture of tilted helices splayed away from the pore lining helices on the cytoplasmic side. (B-D) Representative synthetic nanodisc structures with full length lipids (Rasmussen et al., 2019; Reddy et al., 2019; Zhang et al., 2021) falling into the same category. (E) Peptidisc structure (Angiulli et al., 2020) with similar architecture. (F) An example of MscS in mixed micelles (Flegler et al., 2021) in the same structural category. (G) MscS in full length lipids after cyclodextrin lipid removal (Zhang et al., 2021). (H) The expanded conductive crystal structure of mutant A106V MscS (Wang et al., 2008). (I-J) MscS in synthetic nanodiscs with short lipid chains (Park et al., 2023; Zhang et al., 2021) with a similar architecture to H. (K-L) Representative structures of MscS in detergent (Flegler et al., 2021) in the same structural category as H-J.

Supplemental Table 1: Cryo-EM data collection parameters and analysis.

	Glyco-DIBMA #1	Glyco-DIBMA #2	SMALP 200 #1	SMALP 200 #2	CyclAPol C_8-C_0-50
Date of collection	10/3/2023	11/9/2023	5/9/2023	5/23/2023	10/4/2023
Protein concentration	0.1 mg/mL	0.3 mg/mL	0.3 mg/mL	0.4 mg/mL	0.7 mg/mL
Sample volume	3 µl	3 µl	3 µl	3 µl	3 µl
Double sample application/blot	yes	yes	no	no	no
Grid type	QF R 1.2/1.3 400 Cu mesh + 2nm C	QF R 1.2/1.3 400 Cu mesh + 2nm C	QF R 1.2/1.3 400 Cu mesh + 2nm C	QF R 1.2/1.3 400 Cu mesh + 2nm C	QF R 1.2/1.3 400 Cu mesh + 2nm C
Plunge freezer	Leica EM GP2	Leica EM GP2	Leica EM GP2	Leica EM GP2	Leica EM GP2
Blotting time (s)	6	6	6	6	6
Temperature (°C)	4	4	4	4	4
Humidity (set)	95%	95%	95%	95%	95%
Microscope	Titan Krios G4	Titan Krios G4	Titan Krios G4	Titan Krios G1	Titan Krios G4
Voltage (kV)	300	300	300	300	300
Camera	K3 (non-CDS mode)	K3 (non-CDS mode)	K3 (CDS mode)	K3 (CDS mode)	K3 (non-CDS mode)
Energy filter (slit)	Yes (20 eV)	Yes (20 eV)	Yes (20 eV)	Yes (20 eV)	Yes (20 eV)
Cs corrector	no	no	no	no	no
Objective aperture	no	no	no	100 µm	no
Magnification	105,000x	105,000x	105,000x	105,000x	105,000x
Physical pixel size (Å/px)	0.85	0.85	0.85 (0.425 super-resolution)	0.83 (0.415 super-resolution)	0.85
Electron exposure (e^-/Å^2)	50	50	50	50	50
Number of movie frames	60	60	60	50	60
Dose rate (e^-/px/s)	15	15	10	9	15
Defocus (µm)	-0.8 to -1.7	-0.8 to -1.7	-0.8 to -1.7	-0.8 to -1.8	-0.8 to -1.7
Number of total micrographs	5,604	20,649	2,597	3,100	4,654
Number of selected micrographs	5,604	19,226	1,917	2,937	4,654
Number of particles picked	311,373	3,380,588	47,038	1,177,470	2,911,957

Supplemental Table 2: Cryo-EM map and model analysis.

	Glyco-DIBMA #2 EMD-XXXX PDB ID: XXXX	Glyco-DIBMA #2 EMD-XXXX PDB ID: XXXX
Data processing		
Final number of particles	368,753	368,753
Final pixel size used for final maps (Å/px)	0.85	0.85
Symmetry imposed	C7	C1
Resolution of map (Å)	2.99	3.34
FSC threshold	0.143	0.143
B-factor for map ($Å^2$)	127.8	97.2
Model composition		
Chains	7	7
Non-hydrogen atoms	15,512	15,512
Protein residues	1,855	1,855
Water	98	0
Ligands	28	28
Refinement and validation		
Model resolution (Å)	3.1	3.9
FSC threshold	0.5	0.5
Bond lengths RMSD (Å)	0.002	0.003
Bond angle RMSD (°)	0.441	0.580
MolProbity score	1.63	1.45
Clashscore	7.49	8.33
Rotamer outliers (%)	1.91	0.34
Ramachandran outliers (%)	0.00	0.00
Ramachandran favored (%)	98.48	98.48
Ramachandran allowed (%)	1.52	1.52

Supplemental Table 3: Residues within 5 Å of modelled lipids.

	Lipid 1	Lipid 2	Lipid 3	Lipid 4
Chain A	V29, A33, A36, I37, V40, G41, I44, I77, F80, T81, **R88**	I48, V52, L55, **R59**, L72, V73, G76, I77, F80	V52, L55, M56, **R59, K60,** L69, L72, V73, G104, V107, G108	L69, L72, V107, G108, L111, L115, L118, Q149, I150, F151
Chain B	Y27, N30, I31, L82, L86, **R88**, V89, G90, V91	**D67**, F68, S70, A71, L72, Y75, G76, A79, F80, L100, A103, G104, V107	F68, A71, L72, Y75, V99, A102, A103	T64, V65, **D67**, F68, L72, A103, A106, V107
Chain C		V99		
Chain G				L118, A119, V122, L123, M126, F110

Supplemental Table 4. Summary of patch clamp data. The midpoint ratio of MscS:MscL and the threshold tension were measured in pB113 (*Δ*mscS *Δ*mscK) to compare the mutant MscS to the native MscL, whose tension is taken as 12 mN/m. The percent inactivation and the inactivation recovery τ were measured from plasmids expressing mutants in MJF465 (*Δ*mscS *Δ*mscK *Δ*mscL). Percent inactivation was taken between the initial pulse and the first test pulse in the Inactivation/Recovery Protocol (Figure 4). The recovery from inactivation (τ) is from a fit of the three test pulses to a mono-exponential equation. The numbers in parenthesis indicate the total number of patches. Statistically significant values are indicated with an asterisk.

	γ_{MscS} (mN /m)	**Inactivation (%)**		**Inactivation Recovery τ (s)**	
		+ 30 mV	**- 30 mV**	**+ 30 mV**	**- 30 mV**
WT	7.8	41 ± 26 (10)	74 ± 21 (10)	1.1 ± 0.4 (6)	1.3 ± 0.5 (10)
R88A	7.5 ± 0.7	26 ± 8 (3)	43 ± 5* (3)	2.8 ± 0.5 * (4)	3.5 ± 1.0 (3)
R88Q	9.2 ± 0.4	39 ± 26 (3)	56 ± 25 (3)	1.6 ± 0.8 (3)	1.9 ± 0.8 (3)
R88E	9.2 ± 0.4	60 ± 23 (4)	83 ± 7 (4)	6.6 ± 3.8 (4)	4.1 ± 0.5* (4)
R59A	6.1 ± 0.5	12 ± 8* (3)	25 ± 22* (3)	N/A	N/A
K60A	8.9 ± 1.5	61 ± 24 (4)	78 + 29 (2)	5.8 ± 3.6 (4)	7.5 ± 2.6 (2)
D67A	9.4 ± 0.1	97 ± 5* (7)	99 ± 1* (7)	0.7 ± 0.1* (6)	0.9 ± 0.4* (6)